



HAL
open science

Reactive Rayleigh-Taylor turbulence: Influence of mixing on the growth and displacement of the mixing zone

Kevin Ley, Olivier Soulard, Jérôme Griffond, Antoine Briard, Serge Simoëns

► **To cite this version:**

Kevin Ley, Olivier Soulard, Jérôme Griffond, Antoine Briard, Serge Simoëns. Reactive Rayleigh-Taylor turbulence: Influence of mixing on the growth and displacement of the mixing zone. *Physical Review Fluids*, 2024, 9 (7), pp.074609. 10.1103/PhysRevFluids.9.074609 . hal-04756585

HAL Id: hal-04756585

<https://hal.science/hal-04756585v1>

Submitted on 28 Oct 2024

HAL is a multi-disciplinary open access archive for the deposit and dissemination of scientific research documents, whether they are published or not. The documents may come from teaching and research institutions in France or abroad, or from public or private research centers.

L'archive ouverte pluridisciplinaire **HAL**, est destinée au dépôt et à la diffusion de documents scientifiques de niveau recherche, publiés ou non, émanant des établissements d'enseignement et de recherche français ou étrangers, des laboratoires publics ou privés.

Reactive Rayleigh-Taylor turbulence: Influence of mixing on the growth and displacement of the mixing zone.

Kevin Ley,^{*} Olivier Soulard,[†] Jérôme Griffond, and Antoine Briard
CEA, DAM, DIF, F-91297, Arpajon, France

Serge Simoëns
École Centrale de Lyon, MFAE, LMFA, F-69134 Écully, France

(Dated: June 18, 2024)

The purpose of this paper is to investigate the effects of molecular mixing on the evolution of a reactive Rayleigh-Taylor turbulent mixing zone. In this regard, we derive algebraic relations showing that an increase in the mixing level leads to a slowing down of the growth of the mixing zone width. We also show the existence of a maximum displacement velocity of the mixing zone center. These predictions are assessed using both DNS and LES.

I. INTRODUCTION

The Rayleigh-Taylor instability occurs when two fluids initially separated by an interface are submitted to an acceleration pointing from the denser fluid to the less dense one [1–5]. In this configuration, the small perturbations seeding the initial interface are amplified and eventually develop into a turbulent mixing zone. At late times, this zone reaches a self-similar regime such that its width increases as the square of time. The prefactor α_{nr} of this quadratic evolution is a key parameter of Rayleigh-Taylor turbulence and has been the object of numerous studies [6–17] (note that the subscript “nr” in α_{nr} stands for non-reactive). Among these studies, several point out that α_{nr} is connected to the level of molecular mixing reached in the flow [7–12]. Indeed, the less mixing there is, the more potential energy is available and the faster the growth of the mixing zone should be. As a result, α_{nr} is expected to increase as the level of mixing decreases. This intuitive idea was given a quantitative formulation in Refs. [11, 12]. In these two works, α_{nr} was shown to be a decreasing function of the global mixing parameter Θ , a ratio equal to 0 when the flow is fully segregated and to 1 when it is fully mixed.

In the present work, we consider a Rayleigh-Taylor mixing zone in which chemical or fusion reactions take place [18–34]. Our purpose is to understand whether the level of molecular mixing influences the self-similar evolution of this reactive layer, as it does for a non-reactive one. This question is of importance for several applications, such as, for instance, type Ia supernovae [27–34]. In the latter context, several authors have proposed idealized configurations of Rayleigh-Taylor unstable flames in order to better understand the physical mechanisms at work in these flows. One of the simplest possible setting, studied for instance in [30–34], consists in a statistically planar flame with a small density contrast that propagates upward in a gravity field. The flame is piloted by a single isothermal reaction and consumes heavy reactants initially placed on top of light products. At late times, this unstable flame becomes turbulent and its brush can equivalently be viewed as a turbulent mixing zone driven by the interplay between the Rayleigh-Taylor instability and combustion. It is this idealized flow that we will hereafter examine and refer to as reactive Rayleigh-Taylor turbulence.

The numerical and theoretical studies of [30–33] have put forward several key features of reactive Rayleigh-Taylor turbulence. First, a self-similar regime is reached at late times, such that the width of the mixing zone grows quadratically with time. This is similar to the non-reactive case, except that the prefactor α of this quadratic growth is not necessarily equal to the non-reactive prefactor α_{nr} . Another difference with the non-reactive case is that the center of the mixing zone is not stagnant: it moves towards the reactants as they are being consumed. At late times, the distance traveled by the center is again proportional to the square of time with a prefactor β different from α and α_{nr} . A last key feature highlighted in [30] is that reactions take place in thin flame fronts that separate pockets of pure fluids. The typical size of these fronts increases with time but at a much slower rate than the size of the mixing zone. As a result, the proportion of the volume occupied by mixed regions decreases and the flow becomes more and more segregated: the mixing parameter Θ tends to 0. This is strikingly different from the non-reactive case where high levels of mixing are generally observed with Θ reaching non-zero asymptotic values as high as 0.8 [16].

This last property raises an apparent conundrum concerning the objective of this paper. Indeed, for the non-reactive case, we mentioned that the growth rate of the mixing zone α_{nr} is connected to the level of mixing measured by the

^{*} Also at École Centrale de Lyon, MFAE, LMFA, F-69134 Écully, France

[†] Also at Université Paris-Saclay, CEA, LMCE, Bruyères-le-Châtel 91680, France

value of the mixing parameter Θ [11, 12]. But for the reactive case, the existence of such a dependency appears elusive: the level of mixing vanishes and Θ decreases to 0 whatever the value of the growth rate α . The asymptotic values of α and Θ are consequently independent and, at first sight, it seems that the connection between α and the level of mixing is lost. However, if Θ always tends to 0, it does so in a self-similar fashion, proportionally to the inverse of time and to a non-dimensional parameter γ [30]. Hence, at a given time and for a given reaction rate, a higher γ implies a higher level of mixing. In other words, the mixedness of a self-similar reactive Rayleigh-Taylor flow is measured by the non-zero constant γ and not by the vanishing value of Θ . With this understanding, looking for a dependency of α on the level of mixing remains as legitimate in reactive Rayleigh-Taylor turbulence as it is in the non-reactive case [7–12], provided one substitutes γ to Θ as a measure of the level of mixing. Furthermore, if the growth rate α depends on γ , one may also wonder if it is also the case for the coefficient β measuring the displacement of the mixing zone center.

Thus, the main question we would like to examine in this work can be rephrased as follows : do the growth and displacement rates, α and β , of a self-similar reactive Rayleigh-Taylor mixing zone exhibit any dependency on the degree of mixing of the flow as measured by the constant γ ? To answer this question, we turn our attention to non-reactive Rayleigh-Taylor turbulence and to the $\alpha_{nr} - \Theta$ relation derived in [11, 12]. Two broad assumptions are required to obtain this relation and none of them is specifically tied to the non-reacting character of the flow. Hence, in this work, we propose to start from the very same assumptions as in [11, 12] and to follow their consequences but this time in a reactive setting. More precisely, we assume that an eigenmode of the buoyancy production term is dominant over the other ones and that second order moments are known functions of the mean concentration. Equipped with these hypotheses, we are then able to explore how α , β and γ are related.

The remaining of this paper unfolds as follows. In Sec. II, a general description of reactive Rayleigh-Taylor turbulence, along with its governing equations, is given. Then, in Sec. III, the two assumptions mentioned above are detailed and relationships between α , β and γ are derived. Finally, in Sec. IV, direct numerical simulations (DNS) and large-eddy simulations (LES) are performed. The resolution of these simulations is high enough to attain a state close to self-similarity. Hence, the validity of the results derived in Sec. III can be assessed with these simulations.

II. GENERAL DESCRIPTION OF REACTIVE RAYLEIGH-TAYLOR TURBULENCE

In the introduction, we gave a brief definition of reactive Rayleigh-Taylor turbulence and outlined some of its properties. The aim of this section is to provide further details on this idealized configuration. More precisely, we hereafter present the governing equations of reactive Rayleigh-Taylor turbulence, describe its self-similar regime and draw comparisons with the non-reactive case.

A. Governing equations and global flow parameters

We consider two incompressible fluids that mix and react, while being submitted to a destabilizing gravity field pointing in the direction \mathbf{x}_3 . We assume that the Atwood number of the mixing zone – defined as $A_t = (\rho_h - \rho_l)/(\rho_h + \rho_l)$, with $\rho_{h,l}$ the densities of the “heavy” and “light” fluids – is small compared to one. Besides, for the sake of simplicity, we restrict our attention to the case where the heavy fluid reacts with the light fluid to give even more light fluid. This reaction is auto-catalytic and can be described by adding a Fischer-Kolmogorov-Petrovsky-Piskunov (F-KPP) source term to the evolution of the concentration of the light fluid. Auto-catalytic reactions, and their interaction with the Rayleigh-Taylor instability, play an important role in many industrial applications ([18–23]). The system studied here is consequently directly relevant to these situations. Beyond this aspect, single-step auto-catalytic reactions can also be viewed as toy models for both premixed and non-premixed combustion (see [30] for a discussion on this aspect). This property has been used to gain insights into the behaviour of RT unstable flames and in particular those appearing in SNIa progenitors [27–34]. However, it should be emphasized that a single-step reaction which involves only one scalar cannot describe a configuration where the progress of the reaction is decoupled from the advancement of mixing. At least two scalars would be required in that case. This situation may occur in a wide variety of contexts including some inertial confinement fusion experiments [25, 26, 35]. The study of such configurations is beyond the scope of this work. Note that this limitation is not linked to the particular dependency of the F-KPP source term on the concentration field. The results obtained in this article can be adapted to more complex dependencies, as explained in App. C.

Within this framework, the evolution of the velocity and concentration fields is governed by the following reactive Boussinesq equations:

$$\partial_t c + u_k \partial_k c = \nu_c \partial_{kk}^2 c + \frac{1}{\tau} c(1 - c) \quad (1a)$$

$$\partial_t u_i + u_k \partial_k u_i = -\partial_i p + \nu \partial_{kk}^2 u_i + 2\mathbf{A}_t g c \delta_{i3} \quad , \quad (1b)$$

$$\partial_k u_k = 0 \quad , \quad (1c)$$

99 with \mathbf{u} the velocity field, c the concentration of the light products, g the gravity, p the reduced pressure, ν and ν_c the
100 viscosity and diffusion coefficients and τ the characteristic time of the reaction. In the absence of a turbulent velocity
101 field ($\mathbf{u} = 0$), a laminar flame propagates with a typical velocity s_{lam} and length δ_{lam} defined by:

$$s_{\text{lam}} = 2\sqrt{\nu_c/\tau} \quad \text{and} \quad \delta_{\text{lam}} = 8\sqrt{\nu_c\tau} \quad . \quad (2)$$

102 To complete Sys. (1), initial conditions must be provided. Here, we assume that the light and heavy fluids are initially
103 separated by an interface centered around the position $x_3 = 0$ and deformed by a perturbation of height $h(x_1, x_2)$.
104 With $\mathbf{A}_t g > 0$, the flow is Rayleigh-Taylor unstable provided $c = 1$ for $x_3 < h$ and $c = 0$ for $x_3 > h$:

$$c(\mathbf{x}, t = 0) = \text{Heaviside}(h(x_1, x_2) - x_3) \quad . \quad (3)$$

105 This corresponds to having heavy reactants initially placed above light products. As a result of this convention, the
106 flame propagates towards positive x_3 and the gradient of the mean concentration is negative.

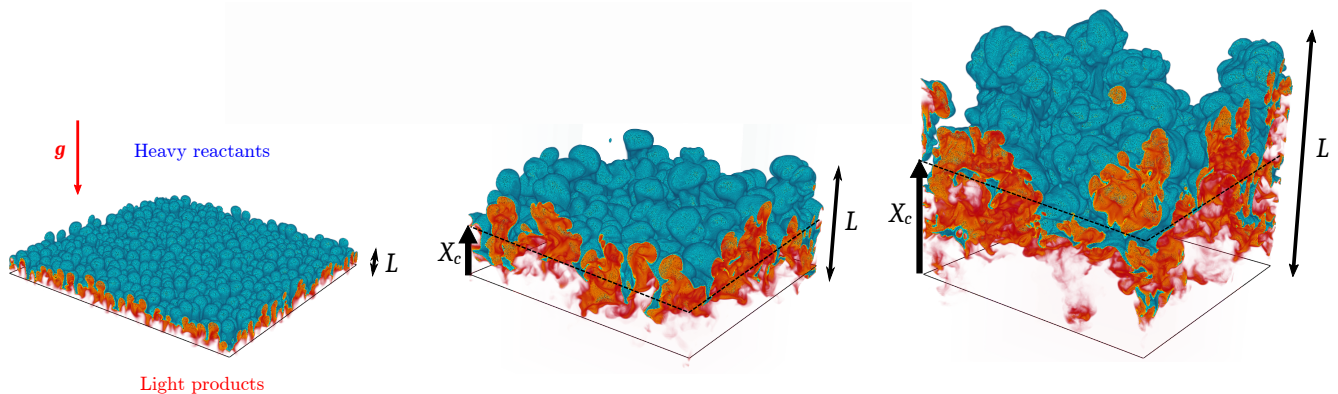


FIG. 1. Typical evolution of a reactive Rayleigh–Taylor flow. Volume rendering of the concentration field c of simulation D2 (see Tab. I) at times $t = 0.8$, $t = 1.9$ and $t = 2.9$. The rendering is done for $0.01 < c < 0.99$. Red corresponds to $c = 0.99$ (light products) and blue to $c = 0.01$ (heavy reactants).

107 A typical evolution of a reactive Rayleigh–Taylor flow obeying Sys. (1) and starting from initial condition (3) is
108 shown in Fig. 1. This figure displays the volume rendering of the concentration field extracted at three different times
109 for simulation D2 that will be detailed in Sec. IV. As we can see, not only does the width L of the mixing zone
110 increase, but its center X_c is also displaced as reactants are consumed. Another important feature of this mixing zone
111 is its high degree of segregation. This can be seen in Fig. 1 by the overwhelming presence of the red and blue colors
112 which correspond to zones of almost pure fluids.

113 These three features – width, displacement and mixing level – can be measured using the following diagnostics:

$$L = 6 \int \bar{c}(1 - \bar{c}) dx_3 \quad , \quad X_c = \int (\bar{c} - \bar{c}^{(0)}) dx_3 \quad \text{and} \quad \Theta = \frac{\int \overline{c(1 - c)} dx_3}{\int \bar{c}(1 - \bar{c}) dx_3} \quad , \quad (4)$$

114 where $\bar{\cdot}$ denotes the ensemble mean and where $\bar{c}^{(0)}(x_3) = \bar{c}(x_3, t = 0)$ is the initial value of \bar{c} . The parameter Θ
115 is called mixing ratio or mixing parameter. Its value falls within the interval $[0, 1]$, $\Theta = 0$ corresponding to a fully
116 segregated flow and $\Theta = 1$ to a fully mixed one. Note that the mixing zone width L is defined up to a multiplicative
117 constant, here chosen equal to 6. Different values can be found in the literature and the choice made here could
118 appear to be arbitrary. However, this is not the case. The reason for selecting a prefactor equal to 6 is linked to the
119 assumptions detailed in section III. They lead to a unique unambiguous value of the prefactor, as explained in App.
120 A.

B. Self-similarity and combustion regime

At late times, Chertkov *et al.* [30] showed that a reactive Rayleigh–Taylor flow obeying Sys. (1) reaches a self-similar state such that:

$$L(t) = 2\alpha A_t g t^2 \quad , \quad X_c(t) = 2\beta A_t g t^2 \quad \text{and} \quad \Theta(t) = \gamma \frac{\tau}{t} \quad , \quad (5)$$

where α , β and γ are three dimensionless constants. Another way of specifying this self-similar regime is by defining dynamic estimates of the coefficients α , β and γ . More precisely, let us introduce the following quantities:

$$\alpha_L(t) = \frac{\dot{L}(t)}{8A_t g \tau_L(t)} \quad , \quad \beta_L(t) = \frac{\dot{X}_c(t)}{8A_t g \tau_L(t)} \quad \text{and} \quad \gamma_L(t) = 2\Theta(t) \frac{\tau_L(t)}{\tau} \quad , \quad (6)$$

where the notation $\dot{f}(t) = d_t f(t)$ is used as a shorthand for the time derivative of a function f depending uniquely on t and where τ_L is the time associated with the growth of the mixing zone width L :

$$\tau_L(t) = \frac{L(t)}{\dot{L}(t)} \quad . \quad (7)$$

Then, the self-similar regime expressed by Eq. (5) can equivalently be defined by:

$$\text{for } t \rightarrow \infty \quad , \quad \alpha_L(t) = \alpha \quad , \quad \beta_L(t) = \beta \quad \text{and} \quad \gamma_L(t) = \gamma \quad . \quad (8)$$

Note that the definition of α_L is identical to the one used classically in non-reactive Rayleigh–Taylor flows. It is however more commonly written in the form $\alpha_L = (\dot{L})^2 / (8A_t g L)$.

Two aspects of the self-similar regime given by Eq. (5) (or equivalently Eq. (8)) are worth highlighting. The first one is that $A_t g$ and t are the only dimensional parameters appearing in the expressions of L and X_c . This implicitly means that buoyancy forces are the primary mechanism driving the growth and displacement of the mixing zone. Nonetheless, the influence of reactions must not be ruled out: they can still have an impact on L and X_c through the values of the constants α and β .

The second remarkable point is that Θ tends to 0, that is, the flow becomes more and more segregated with time. In [30], this behaviour was associated with the emergence of a thickened-wrinkled flame combustion regime [36]. As its name indicates, this regime corresponds to reaction zones that are broadened by the smallest scales of the turbulent spectrum, while also being wrinkled by the largest ones. Chertkov *et al.* [30] showed that, in reactive Rayleigh–Taylor turbulence, the broadening of the reaction zones is slower than the growth of the mixing zone width. Hence, the volume they occupy becomes smaller and smaller compared to the volume occupied by the burnt and unburnt fluids. This results in Θ tending to 0.

It should be emphasized that the tendency towards the thickened-wrinkled regime is a direct consequence of the self-similar evolution expressed by Eq. (5). More precisely, the thickened-wrinkled flame regime is defined by high values of two non-dimensional numbers, the Damköhler and Karlovitz numbers, which compare the reaction time τ to the characteristic times τ_t and τ_η of the largest and smallest structures of the turbulent field. These two numbers are defined as $\text{Da} = \tau_t / \tau$ and $\text{Ka} = \tau / \tau_\eta$. During the self-similar phase, with $A_t g$ and t the only dimensional parameters involved, we necessarily have $\tau_t \propto t$. Furthermore, assuming a Kolmogorov turbulent spectrum, we have $\tau_\eta \propto \tau_t \text{Re}^{-1/2} \propto t^{1/2}$, with Re the turbulent Reynolds number. Therefore, once the self-similar phase is reached, Da and Ka grow with time and eventually become very large: the thickened-wrinkled flame regime is reached.

This property can be illustrated using a Borghi diagram, which allows to visualize the different combustion regimes in a velocity-length scale phase space. Figure 2 shows such a Borghi diagram in which the typical turbulent velocity v' and length scale ℓ_t at the center of the mixing zone and for different times are reported for simulations D1, D2, D3, D4 detailed in Sec. IV. Once self-similarity is reached, we have $v' \propto t$ and $\ell_t \propto t^2$ so that $v' \propto \ell_t^{1/2}$. In other words, a self-similar evolution of these quantities appears in the Borghi diagram as a curve with a logarithmic slope 1/2. This property is indeed observed for simulations D1, D2, D3, D4 in Fig. 2. It can also be observed in this figure that a 1/2-slope curve always ends up within the boundaries of the thickened-wrinkled flame region as time increases. This region is indeed delimited by the two curves $\text{Da} = 1$ and $\text{Ka} = 1$, which respectively have logarithmic slopes of 1 and 1/3.

C. Comparison with non-reactive Rayleigh–Taylor turbulence

Without reaction, the self-similar state of Rayleigh–Taylor turbulence is characterised by the following relations:

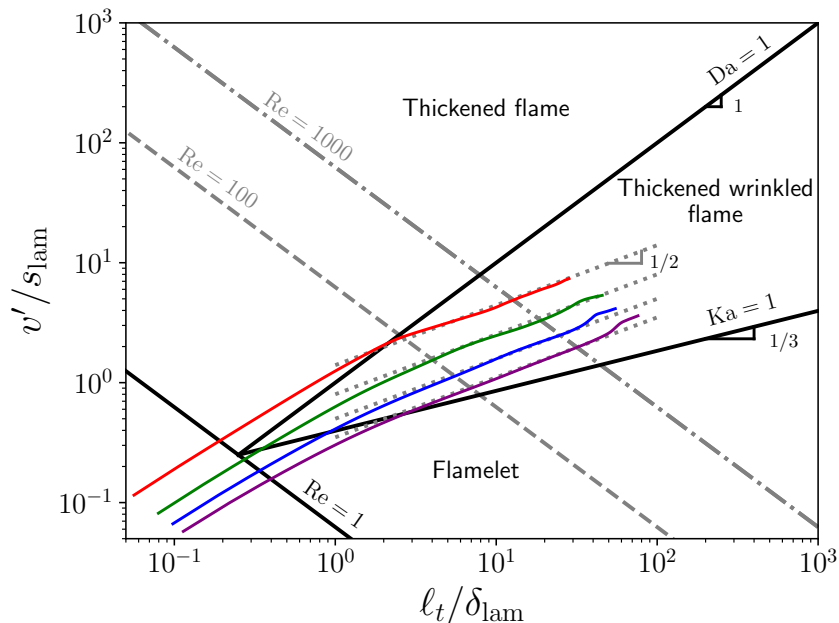


FIG. 2. Borghi diagram for simulations D1 (red), D2 (green), D3 (blue) and D4 (purple) (see Tab. I for simulation names). The curve shown for each simulation is obtained by plotting $[\ell_t(t)/\delta_{\text{lam}}, v'(t)/s_{\text{lam}}]$ for different times t . The turbulent velocity v' corresponds to the square root of the turbulent kinetic energy taken at the center of the mixing zone. The integral scale ℓ_t is computed by integrating the turbulent velocity spectrum divided by the wave number and normalized by the kinetic energy. The definitions of the laminar flame speed and width are given in Eq. (2).

$$\text{Non-reactive case: } L = 2\alpha_{\text{nr}}\text{At}g^2 \quad , \quad X_c = 0 \quad \text{and} \quad \Theta = \Theta_\infty \quad , \quad (9)$$

163 where α_{nr} and Θ_∞ are dimensionless constants.

164 The comparison between Eqs. (5) and (9) reveals several differences between reactive and non-reactive Rayleigh–
 165 Taylor turbulence. First, even though the growth of the mixing zone is quadratic in time in both cases, the growth
 166 constants α and α_{nr} of the two flows are not necessarily the same. Second, the center of the mixing zone does not
 167 move in the absence of reaction. And finally, without reactions, the mixing parameter Θ tends to a non-zero constant
 168 Θ_∞ . Simulations [4] suggest that Θ_∞ is close to 0.8, which corresponds to a well-mixed flow. This is in stark contrast
 169 with the reactive case for which the mixture becomes almost fully segregated. This last point, more than any other,
 170 sets apart the reactive and non-reactive versions of the Rayleigh–Taylor instability.

171 Indeed, mixing plays an important role in understanding the behaviour of Rayleigh–Taylor turbulence. As explained
 172 in the introduction, a lesser level of molecular mixing implies that more potential energy is available and can be
 173 converted into kinetic energy, which, in turn, can contribute to the growth of the mixing zone. This simple and
 174 intuitive reasoning connects the growth of the mixing zone to the level of mixing. It does not depend on whether
 175 reactions are present or not and, if verified, should apply equally well to non-reactive and reactive Rayleigh–Taylor
 176 turbulence.

177 For non-reactive Rayleigh–Taylor turbulence, this connection has been corroborated and translated in the form of
 178 a relation between the dynamic evaluation α_L of the growth coefficient (Eq. (6)) and the mixing parameter Θ [11, 12]:

$$\alpha_L(t) = \frac{(d_{cc}(1 - \Theta(t)))^2}{1 + d_{cc}(1 - \Theta(t))} \quad . \quad (10)$$

179 At large times, we have $\alpha_L(t) \rightarrow \alpha_{\text{nr}}$ and $\Theta(t) \rightarrow \Theta_\infty$ so that the asymptotic version of Eq. (10) is :

$$\alpha_{\text{nr}} = \frac{(d_{cc}(1 - \Theta_\infty))^2}{1 + d_{cc}(1 - \Theta_\infty)} \quad . \quad (11)$$

180 In formula (10) and (11), $d_{cc} \in [0, 1]$ is an anisotropy coefficient which measures whether turbulent structures are
 181 flat or elongated. It is equal to $\pi/4$ in the isotropic case and to 1 for fully elongated structures. A value of 0.7 to
 182 0.8 is generally observed in non-reactive Rayleigh–Taylor simulations [11, 12]. In [11], d_{cc} is approximated by $d_{cc} =$

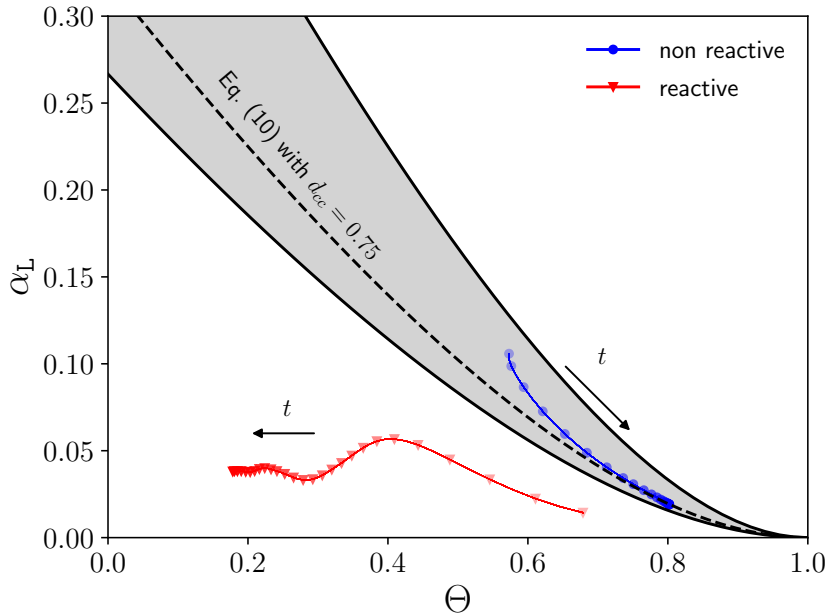


FIG. 3. Comparison between reactive (Sim. D2) and non-reactive (Sim. NR) Rayleigh–Taylor turbulence (see Tab. I for simulation names). Growth coefficient α_L as a function of the mixing parameter Θ for an interval of time such that L/L_{dom} varies between 0.02 and 0.3 for Sim. D2 and between 0.05 and 0.3 for Sim. NR. The opacity of the symbols increases with time. The two black curves are obtained by setting $d_{cc} = 1$ and $d_{cc} = 2/3$ in Eq. (10). The gray region they delimit corresponds to the $(\alpha_L - \Theta)$ domain identified in [11] as encompassing most simulation and experimental results of non-reactive Rayleigh–Taylor turbulence.

183 $\int E_{cc}(\mathbf{k}) \sin^2 \theta d\mathbf{k} / \int E_{cc}(\mathbf{k}) d\mathbf{k}$ where E_{cc} is the concentration spectrum, \mathbf{k} the wave number and $\theta = \arccos(k_3/k)$ the
 184 angle between \mathbf{k} and \mathbf{x}_3 . In [12], a more complex formula involving eigenmode spectra is used.

185 Equation (10) is assessed in Fig. 3 using the non-reactive Rayleigh–Taylor simulations described in Sec. IV. It can
 186 be seen that the simulation results align with the predicted curve defined by Eq. (10) with $d_{cc} = 0.7$. In addition to
 187 these non-reactive data, Fig. 3 also displays results for the reactive simulation D2 described in Sec. IV. As expected
 188 from Eqs. (5) and (9), the (α_L, Θ) trajectories of the reactive and non-reactive cases are blatantly different and formula
 189 (10) clearly does not apply to reactive Rayleigh–Taylor turbulence. In the reactive case, an almost horizontal line is
 190 obtained: α_L reaches an asymptotic value, while Θ still decreases with time. This horizontal line is an illustration of
 191 the fact that no univocal relation between α_L and Θ can be drawn in the reactive case.

192 At first sight, this observation may appear to contradict the existence of a connection between growth rate and
 193 mixing levels in the reactive case. However, it only shows that this connection does not take the form of a $\alpha_L - \Theta$
 194 relationship. Given the properties (5) of the reactive self-similar state, α_L and its asymptotic value α still appear as
 195 proper parameters for estimating the growth of the mixing zone. However, the fact that Θ tends to 0 means that this
 196 parameter is not fit for comparing mixing levels. Instead, it is the prefactor γ of the decay law of Θ that now plays
 197 this role: at a given non-dimensional time t/τ , different values of γ imply different degrees of mixing.

198 Thus, for reactive Rayleigh–Taylor turbulence, the link between growth rate and mixing should not be looked for in
 199 the form of a relation between α and Θ but rather between α and γ , or equivalently between α_L and γ_L , the dynamic
 200 estimates of α and γ (Eq. (6)). The same remark also applies to β and β_L . To derive these relations, several hypotheses
 201 are required. They are detailed in the next section, along with their consequences.

202 III. RELATIONSHIPS BETWEEN α , β AND γ

203 A. Overview of the derivation

204 1. Main steps of the derivation

205 The derivation presented in this section hinges around one central quantity : the mean concentration \bar{c} . The latter

206 evolves according to the following equation, obtained by averaging Eq. (1a) :

$$\partial_t \bar{c} + \partial_3 \overline{u_3' c'} = \nu_c \partial_{33}^2 \bar{c} + \frac{1}{\tau} \overline{c(1-c)} \quad , \quad (12)$$

207 with $X' = X - \bar{X}$ the fluctuation of a given quantity X . The reason why \bar{c} plays such an important role is because
 208 the knowledge of its self-similar properties allows to formulate two independent equations linking α , β and γ . It thus
 209 brings an answer to the problem raised in the preceding section, namely finding how the growth and displacement
 210 rates of the mixing zone, α and β , depend on the mixing level measured by γ .

211 The first of these two equations is obtained rather straightforwardly. By integrating Eq. (12) over x_3 , the following
 212 equation for X_c is derived:

$$\dot{X}_c = \frac{\Theta L}{6\tau} \quad , \quad (13)$$

213 where we used the definitions of X_c , Θ and L (Eq. (4)) and the fact that the molecular and turbulent concentration
 214 fluxes are null outside the mixing zone. Injecting the self-similar evolution of X_c , Θ and L (Eq. (5)) into this equation,
 215 we then find that:

$$\beta = \frac{\gamma}{12} \alpha \quad . \quad (14)$$

216 As for the second relation, its starting point rests on the following observation: once self-similarity is reached, the mean
 217 concentration profile depends only the dimensionless coordinate x_3/L and on non-dimensional self-similar parameters.
 218 These include α , β and γ but are not limited to them. This property can be expressed as:

$$\text{Self-similar regime :} \quad \bar{c}(t, x_3) \equiv \bar{c}_s \left(\frac{x_3}{L(t)}; \alpha, \gamma, \mathbf{p} \right) \quad , \quad (15)$$

219 where $\mathbf{p} = (p_1, p_2, \dots)$ stands for the ensemble of the self-similar parameters other than α and γ . The parameter β is
 220 not included due to its explicit dependency on α and γ (Eq. (14)). When injecting this expression into the definition
 221 (4) of L , i.e into $L = 6 \int \bar{c}(1 - \bar{c}) dx_3$, and when replacing the integration variable by $y = x_3/L$, we derive that:

$$\mathcal{I}(\alpha, \gamma, \mathbf{p}) = 1 \quad (16a)$$

$$\text{with} \quad \mathcal{I}(\alpha, \gamma, \mathbf{p}) = 6 \int \bar{c}_s(y; \alpha, \gamma, \mathbf{p}) (1 - \bar{c}_s(y; \alpha, \gamma, \mathbf{p})) dy \quad . \quad (16b)$$

222 Thus, an integral equation is obtained, which links α , γ and the other self-similar parameters \mathbf{p} together. When
 223 solved, this equation allows to express α as a function of γ and \mathbf{p} :

$$\alpha \equiv \alpha_s(\gamma, \mathbf{p}) \quad . \quad (17)$$

224 Formally, this solution would answer the main question raised in our paper.

225

2. Main assumptions

226 To sum up, Eq. (17) is the main relation we aim to derive. To this end the value of $\mathcal{I}(\alpha, \gamma, \mathbf{p})$ must first be
 227 found. And for this, it is necessary to determine the self-similar profile \bar{c}_s of \bar{c} . This may only be accomplished by
 228 introducing simplifying assumptions. In this regard, it is instructive to consider the non-reactive case and the way
 229 Eqs. (10) and (11) were obtained in [11, 12]. In these references, two main hypotheses were necessary to arrive at
 230 these predictions. The first one is that buoyancy production plays a dominant role at energetic scales and the second
 231 that the spatial profile of the mean concentration \bar{c} is linear within the mixing zone. In [11], it was also explained how
 232 this second hypothesis is fully equivalent to specifying that the spatial profiles of the variance and flux of concentration
 233 are proportional to $\bar{c}(1 - \bar{c})$.

234 Concerning the reactive case, we already noted in Sec. IIB that buoyancy forces are the main mechanism driving the
 235 growth and displacement of the mixing zone, as implied by the dimensional parameters appearing in the self-similar
 236 laws (5). This suggests that the first hypothesis mentioned above should remain appropriate for analysing reactive
 237 Rayleigh–Taylor turbulence. As for the second hypothesis, its alternative formulation based on second order moments
 238 can be viewed as a truncation of their spatial profiles in terms of Legendre polynomials. Its principle is consequently
 239 not restricted to the non-reactive case and its implications can also be explored in a reactive context.

240 Thus, despite the intrinsic differences between reactive and non-reactive Rayleigh–Taylor flows, the study of the
 241 way growth rate and mixing are linked can be approached using the same general assumptions. These assumptions,
 242 however, have very different consequences in each context. This is what we detail in the remaining of this section.

243

B. First assumption: truncated Legendre polynomial expansion

244

1. Legendre expansion

245 First of all, let us recast the evolution equation of \bar{c} by using the self-similar coordinate $y = x_3/L$, already introduced
246 in the definition of $\mathcal{I}(\alpha, \gamma, \mathbf{p})$. We obtain:

$$\tau_L \partial_t \bar{c} - y \partial_y \bar{c} + \partial_y \left(\overline{u'_3 c'} / V_L \right) = \frac{1}{\text{Sc} \cdot \text{Re}_L} \partial_{yy}^2 \bar{c} + \text{Da}_L \overline{c(1-c)} \quad (18)$$

$$\text{with } V_L = \dot{L} \quad , \quad \text{Sc} = \frac{\nu}{\nu_c} \quad , \quad \text{Re}_L = \frac{L V_L}{\nu} \quad \text{and} \quad \text{Da}_L = \frac{\tau_L}{\tau} \quad . \quad (19)$$

247 We recall that $\tau_L = L/V_L$ has already been introduced in Eq. (7) in order to define α_L , β_L and γ_L . Three non-
248 dimensional numbers appear in Eq. (18): the Schmidt number Sc , the Reynolds number Re_L and the Damköhler
249 number Da_L . The latter two are based on the width L and on the velocity $V_L = \dot{L}$ and are different from the turbulent
250 Reynolds and Damköhler numbers, Re and Da , which were introduced in Sec. II.

251 By itself, Eq. (18) is not sufficient to make any statement about the shape of \bar{c} . Two unknown correlations, the
252 flux of concentration $\overline{u'_3 c'}$ and its variance $\overline{c'^2} = \overline{c(1-c)} - \overline{c(1-c)}$, are indeed involved in Eq. (18). In order to deal
253 with these correlations, we note that, within the bounds of the mixing zone, the mean concentration $\bar{c}(t, y)$ varies
254 monotonically as a function of y . Hence, within these bounds, i.e for $0 < \bar{c}(t, y) < 1$, we may invert the dependency
255 of $\bar{c}(t, y)$ on y and write that y is a function of \bar{c} :

$$\text{for } 0 < \bar{c} < 1 \quad , \quad y \equiv f(t, \bar{c}) \quad . \quad (20)$$

256 Plugging this dependency into the two unknown correlations, we obtain that:

$$\text{for } 0 < \bar{c} < 1 \quad , \quad \frac{\overline{u'_3 c'}}{V_L} = F(t, \bar{c}) \quad \text{and} \quad \overline{c(1-c)} = V(t, \bar{c}) \quad . \quad (21)$$

257 With $\overline{u'_3 c'}$ a function of \bar{c} , the turbulent transport term of Eq. (18) can be recast in the form of an advection term,
258 with an advection velocity equal to $F'(t, \bar{c}) = \partial_{\bar{c}} F(t, \bar{c})$. Then, in order for the edges of the mixing zone to move at
259 a non-zero finite velocity, F' must tend to a non-zero finite value when $\bar{c} \rightarrow 0$ and $\bar{c} \rightarrow 1$. As a result, F must be
260 proportional to \bar{c} for $\bar{c} \rightarrow 0$ and to $1 - \bar{c}$ for $\bar{c} \rightarrow 1$. Furthermore, the Schwartz inequality implies that $\overline{c(1-c)}$ is
261 smaller than $\overline{c(1-c)}$. Hence, it goes to 0 at most like \bar{c} for $\bar{c} \rightarrow 0$ and like $1 - \bar{c}$ for $\bar{c} \rightarrow 1$. A general expansion
262 satisfying these boundary conditions can be written using associated Legendre polynomials of order 2:

$$F(t, \bar{c}) = \bar{c}(1 - \bar{c}) \left[F_0(t) + F_1(t) \tilde{P}_1(\bar{c}) + \dots + F_n(t) \tilde{P}_n(\bar{c}) + \dots \right] \quad , \quad (22a)$$

$$V(t, \bar{c}) = \bar{c}(1 - \bar{c}) \left[V_0(t) + V_1(t) \tilde{P}_1(\bar{c}) + \dots + V_n(t) \tilde{P}_n(\bar{c}) + \dots \right] \quad , \quad (22b)$$

263 where \tilde{P}_n is a modified associated Legendre polynomial of second order and degree n :

$$\tilde{P}_n(x) = \sqrt{\frac{(2n+5)n!}{30(n+4)!}} \frac{P_{n+2}^{(2)}(2x-1)}{x(1-x)} \quad , \quad (23)$$

264 with $P_{n+2}^{(2)}$ the actual associated Legendre polynomial of second order and degree $n+2$.

265

2. Truncation of the Legendre expansion

266 Expansion (22) does not involve any approximation and injecting it as such in Eq. (18) would not allow to make
267 any progress in our derivation: a simplification is needed. This is where we introduce the first of the two major
268 hypotheses mentioned at the beginning of this section. Namely, we assume that the main order of these developments
269 is much larger than the remaining terms:

$$\text{for } i \geq 1 \quad , \quad F_i \ll F_0 \quad \text{and} \quad V_i \ll V_0 \quad . \quad (24)$$

270 As a result, we propose to approximate the profile of $\overline{u'_3 c'}$ and $\overline{c(1-c)}$ by keeping the sole contribution of the main
271 order. Reintroducing y as the dependent variable, this allows to write that:

$$\frac{\overline{u'_3 c'}}{V_L}(t, y) = \overline{c}(t, y) (1 - \overline{c}(t, y)) F_0(t) \quad \text{and} \quad \overline{c(1-c)}(t, y) = \overline{c}(t, y) (1 - \overline{c}(t, y)) V_0(t) \quad . \quad (25)$$

272 The coefficient V_0 can be determined by integrating $\overline{c(1-c)}$ over y . Given the definition of Θ in Eq. (4), we
273 straightforwardly find that:

$$V_0(t) = \Theta(t) \quad . \quad (26)$$

274 As for F_0 , its expression will be the object of the next section. For the time being, this coefficient can be put aside
275 by introducing a new non-dimensional coordinate z defined by:

$$z = \frac{y}{2F_0} = \frac{1}{2F_0} \frac{x_3}{L} \quad . \quad (27)$$

276

3. Self-similar profile of \overline{c}

277 We now inject the truncated Legendre expansion (25) into the evolution equation (18) of \overline{c} and use the new
278 coordinate z . But instead of handling directly the equation giving \overline{c} as a function of z , we consider the corresponding
279 equation giving z as a function of \overline{c} . As before, this operation is possible because we restrict our attention to the
280 domain $\overline{c}(1-\overline{c}) \neq 0$ where \overline{c} is a strictly monotonous function of z . So, for $0 < \overline{c} < 1$, we derive that $z(t, \overline{c})$ evolves as:

$$\tau_L \partial_t z + \frac{\gamma_L}{2} \overline{c}(1-\overline{c}) \partial_{\overline{c}} z = - \left(z \left(1 + \tau_L \dot{F}_0 / F_0 \right) + \overline{c} - \frac{1}{2} \right) + \frac{1}{4F_0^2 \text{Sc} \cdot \text{Re}_L} (\partial_{\overline{c}} z)^{-2} \partial_{\overline{c}}^2 z \quad . \quad (28)$$

281 In the self-similar regime, the following relations hold:

$$\partial_t z(t, \overline{c}) = 0 \quad , \quad \dot{F}_0 = 0 \quad , \quad \text{Re}_L \rightarrow \infty \quad \text{and} \quad \gamma_L = \gamma \quad . \quad (29)$$

282 As a result, in the self-similar regime, Eq. (28) simplifies to:

$$\frac{dz}{d\overline{c}} = - \frac{2z + \overline{c} - \frac{1}{2}}{\gamma \overline{c}(1-\overline{c})} \quad . \quad (30)$$

283 The solution of this equation is:

$$z_s(\overline{c}; \gamma) = \frac{1}{2} - \frac{2\overline{c}}{2 + \gamma} {}_2F_1(1, 1; 2 + 2/\gamma; \overline{c}) \quad , \quad (31)$$

284 where ${}_2F_1(a_1, a_2; b_1; x)$ is the Gauss hypergeometric function with parameters a_1, a_2, b_1 and variable x . By inverting
285 this expression, we eventually obtain \overline{c}_s , the self-similar profile of \overline{c} , as a function of z and γ :

$$\overline{c}_s(z; \gamma) = z_s^{-1}(z; \gamma) \quad . \quad (32)$$

286 In the general case, finding the inverse z_s^{-1} of z_s cannot be done analytically and requires numerical means. Nonethe-
287 less, several remarkable properties of \overline{c}_s can still be put forward. In particular, the range over which \overline{c}_s is strictly
288 different from 0 and 1 extends symmetrically with respect to $z = 0$, from $z = -1/2$ to $z = +1/2$. However, between
289 these symmetric bounds, the self-similar profile of \overline{c} can be strongly asymmetric, depending on the value of γ . To
290 illustrate this point, we may consider two asymptotic limits : $\gamma \rightarrow 0$ and $\gamma \rightarrow \infty$. For $\gamma \rightarrow 0$, the hypergeometric
291 function ${}_2F_1(1, 1; 2 + 2/\gamma; \overline{c})$ appearing in Eq. (31) tends to 1 so that the self-similar profile of \overline{c} becomes linear and
292 symmetric with respect to $z = 0$:

$$\text{for } \gamma \rightarrow 0 \quad , \quad \overline{c}_s = \frac{1}{2} - z \quad . \quad (33)$$

293 By contrast, when $\gamma \rightarrow \infty$, ${}_2F_1(1, 1; 2 + 2/\gamma; \overline{c})$ tends to $-(\ln(1-\overline{c}))/\overline{c}$. As a result, we have:

$$\text{for } \gamma \rightarrow \infty \quad , \quad \overline{c}_s = 1 - e^{-\frac{\gamma}{4}(1-2z)} \quad . \quad (34)$$

294 Thus, for large γ , \overline{c}_s is close to a step: it is almost equal to 1 over most of the interval $[-1/2, 1/2]$ and goes to 0 over
295 a small sub-interval located close to $z = 1/2$.

4. The length scales of \bar{c}_s and their ratio

296

297 Fig. 4(a) shows how \bar{c}_s transitions from a linear to a step-like profile with increasing γ . Because of this behaviour,
 298 a single length scale is not sufficient to characterize the profile of \bar{c}_s . Indeed, as γ increases, the size of the domain
 299 where \bar{c}_s is strictly different from 0 and 1 disconnects from the size of the fast varying front of \bar{c}_s : the ratio between
 300 the latter and the former goes to 0.

301 More precisely, the support of \bar{c}_s extends from $-1/2$ to $1/2$ in terms of the non-dimensional variable $z = x_3/(2F_0L)$.
 302 In dimensional units, this means that the total extent of the concentration profile is:

$$H = 2F_0L \quad . \quad (35)$$

303 Besides, the definition (4) of L entails that the latter scale only measures the part of the domain where \bar{c}_s is significantly
 304 different from 0 and 1. In other words, L gives a measure of the fast varying front of \bar{c}_s . The ratio between L and H
 305 can be evaluated by simply changing the integration variable from x_3 to z in the definition (4) of L . By doing so, we
 306 derive that:

$$\frac{L}{H} = \mathcal{G}(\gamma) = 6 \int_{-1/2}^{1/2} \bar{c}_s(z; \gamma)(1 - \bar{c}_s(z; \gamma))dz \quad . \quad (36)$$

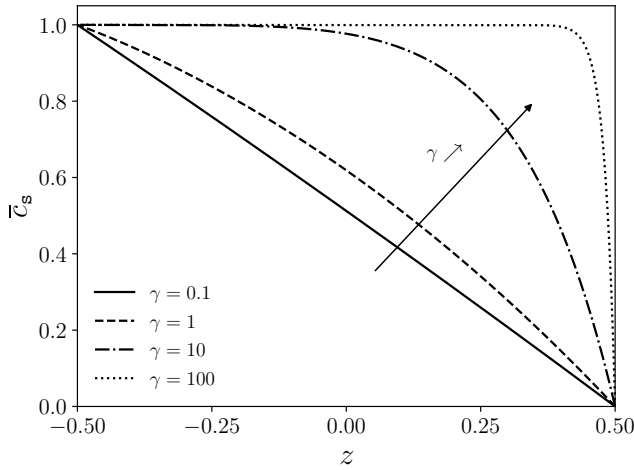
307 Changing again the integration variable, this time from z to $c = c_s(z; \gamma)$, we obtain that

$$\mathcal{G}(\gamma) = 6 \int_0^1 c(1-c) \left| \frac{dz_s}{dc} \right| (c) dc = \frac{12}{\gamma} \int_0^1 z_s(c; \gamma) dc \quad , \quad (37)$$

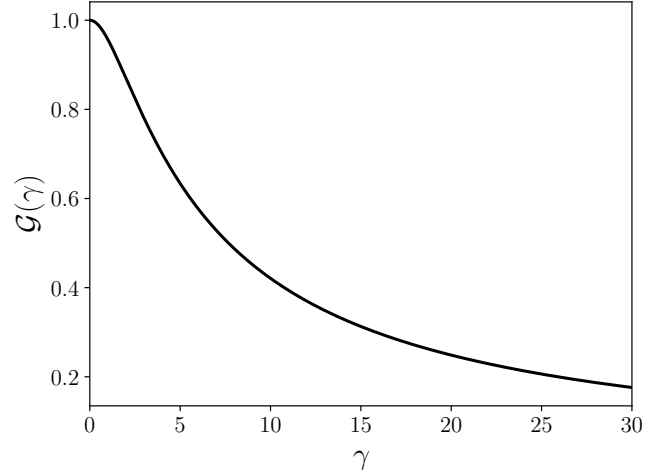
308 where, in the second equality, we used the definition (30) of dz_s/dc and the fact that $\int_0^1 (c - 1/2)dc = 0$. Finally,
 309 injecting the hypergeometric expression (31) of z_s into this equation, we reach the following result:

$$\mathcal{G}(\gamma) = \frac{6}{\gamma} \left(1 - \frac{4}{\gamma} \left(1 - \frac{2}{\gamma} \Psi^{(1)} \left(1 + \frac{2}{\gamma} \right) \right) \right) \quad , \quad (38)$$

310 where $\Psi^{(1)}(x) = \frac{d^2 \ln \Gamma(x)}{dx^2}$ is the trigamma function.



(a) Self-similar profile of \bar{c} as a function of z for different values of γ .



(b) Variation of $\mathcal{G} = L/H$ as a function of γ .

FIG. 4. Self-similar profile of \bar{c} and associated length scale ratio.

311

312

313 The function \mathcal{G} is displayed in Fig. 4(b). It is strictly decreasing and has values in the interval $[0, 1]$. It verifies:

$$\mathcal{G}(0) = 1 \quad \text{and} \quad \text{for } \gamma \gg 1 \quad , \quad \mathcal{G}(\gamma) = 6/\gamma \quad .$$

314 Thus, the two length scales L and H only coincide for small values of γ . For large values of γ , L becomes much
 315 smaller than H : a fast-varying front is formed with a size of order γ^{-1} relative to the total extent of the mixing zone.

316 An important point is that H not only gives the size of the domain where $\bar{c} \in]0, 1[$. It also gives the minimum
 317 extent of the region where the turbulent kinetic energy is not null. Otherwise, $\overline{u'_3 c'}$ could not be proportional to
 318 $\bar{c}(1 - \bar{c})$. As a result, for large γ , the size L of the front where \bar{c} varies rapidly becomes much smaller than the size
 319 occupied by the turbulent field itself. Besides, for large γ , buoyancy production concentrates within the front, which
 320 has large mean concentration gradients, and becomes almost null outside of it. Hence, turbulence can be thought to
 321 be generated within the front and then left to decay and diffuse outside of it as the front advances.

322 C. Second assumption: predominance of the enhanced buoyancy eigenmode

323 With Eq. (32), we have succeeded in deriving an expression for the self-similar profile \bar{c}_s of the mean concentration \bar{c} .
 324 This result is a step forward in our search for the value of $\mathcal{I}(\alpha, \gamma, \mathbf{p})$ that will eventually enable us to link α and γ .
 325 However, Eq. (32) alone is not sufficient to fulfill this objective. The reason is that, in Eq. (32), \bar{c}_s is expressed as
 326 a function of the non-dimensional variable z , and not of the variable y appearing in the definition (16b) of \mathcal{I} . With
 327 $y = z/(2F_0)$, this difference means that F_0 appears as an unknown parameter when combining Eqs. (32) and (16b).
 328 To overcome this issue and derive a closed expression for F_0 , an additional assumption is required. The description
 329 of this hypothesis and of its consequences is the subject of this subsection.

330 1. Predominance of the growing mode

331 To begin with, let us recall that F_0 is the coefficient of the main order of the Legendre expansion (22) of the
 332 concentration flux $\overline{u'_3 c'}$. Given our first approximation and the possibility to truncate this expansion, F_0 can also be
 333 recast as a function of the integral of $\overline{u'_3 c'}$. Integrating Eq. (25) over y , we find that:

$$F_0 = \frac{6\langle \overline{u'_3 c'} \rangle}{V_L} \quad \text{with} \quad \langle \cdot \rangle = \int \cdot \, dy = \frac{1}{L} \int \cdot \, dx_3 \quad . \quad (39)$$

334 So to find F_0 , we need to evaluate the spatial average of the concentration flux $\langle \overline{u'_3 c'} \rangle$.

335 In non-reactive Rayleigh–Taylor turbulence [12, 17], this quantity is modelled by considering that the dynamics of
 336 the mixing zone at energetic scales is driven by buoyancy production. For reactive turbulence, we follow the same
 337 path. Even though reactions strongly modify the state of the mixture by creating pockets of light and heavy fluids,
 338 we assume that the growth of the mixing zone is determined by the way these pockets of pure fluids move relatively to
 339 one another under the action of buoyancy forces. As already noted, this assumption is coherent with the self-similar
 340 scalings (5) of L and X_c which only depend on $\mathbf{A}_t g$ and t .

341 This phenomenological description about the role played by buoyancy production is translated in quantitative
 342 terms as follows. In Boussinesq Rayleigh–Taylor turbulence, whether reactive or not, buoyancy production takes
 343 the form of a linear system acting on \mathbf{u}' and c' . Setting aside the spatial variations of $\partial_3 \bar{c}$, this system possesses
 344 three homogenized eigenmodes, a_+ , a_0 and a_- . Among these modes, only a_+ is associated with a positive eigenvalue
 345 and is consequently enhanced by buoyancy production. The other two are either inhibited (a_-) or neutral (a_0). In
 346 non-reactive Rayleigh–Taylor turbulence [12, 17], this enhanced mode is found to be highly dominant over the other
 347 ones for large and energetic scales. Our assumption –the second major assumption of this work– is that it is also the
 348 case for reactive Rayleigh–Taylor turbulence. In particular, we assume that the variance of the enhanced mode is
 349 large compared to the correlations involving the other modes:

$$\langle \overline{a_+^2} \rangle \gg \langle \overline{a_p a_q} \rangle \quad \text{with} \quad p, q \in \{0, -\} \quad . \quad (40)$$

350 2. Relation between F_0 and α

351 Now, the velocity and concentration fields \mathbf{u}' and c' can be expressed as linear combinations of a_+ , a_- and a_0 in
 352 spectral space. This linear dependency extends to turbulent spectra and, from there, to second order correlations.
 353 Following [12], we can write that:

$$\frac{\langle \overline{u'_3 c'} \rangle}{V_L} = M_{pq} \langle \overline{a_p a_q} \rangle \quad \text{and} \quad \langle \overline{c'^2} \rangle = N_{pq} \langle \overline{a_p a_q} \rangle \quad , \quad (41)$$

354 where $p, q \in \{+, -, 0\}$ and where M_{pq} and N_{pq} are matrices which depend on α_L and on the angular properties

355 of the spectra of the eigenmodes [12]. Using assumption (40) and retaining only the dominant term, we can then
 356 approximate these expressions by:

$$\frac{\langle u'_3 c' \rangle}{V_L} = M_{++} \langle a_+^2 \rangle \quad \text{and} \quad \langle c'^2 \rangle = N_{++} \langle a_+^2 \rangle \quad . \quad (42)$$

357 Combining these two equalities and using the relation $\langle c'^2 \rangle = (1 - \Theta)/6$, we thus find that:

$$\frac{\langle u'_3 c' \rangle}{V_L} = \frac{1}{6} \frac{M_{++}}{N_{++}} (1 - \Theta) \quad . \quad (43)$$

358 In [12], the multiplicative factor in front of $1 - \Theta$ was determined and found to be equal to:

$$\frac{M_{++}}{N_{++}} = \frac{d_{cc}}{\alpha_L + \sqrt{4\alpha_L + \alpha_L^2}} \quad , \quad (44)$$

359 where $d_{cc} \in [0, 1]$ is the exact same parameter as the one appearing in Eqs. (10) and (11). Let us recall that
 360 d_{cc} characterizes the directional anisotropy of the spectrum of a_+ and tells whether turbulent structures are flat or
 361 elongated.

362 Combining Eqs. (39), (43) and (44) we eventually arrive at the following expression for F_0 :

$$F_0 = \frac{d_{cc}}{\alpha_L + \sqrt{4\alpha_L + \alpha_L^2}} (1 - \Theta) \quad . \quad (45)$$

363 This expression only assumes the predominance of the growing mode and is not restricted to the self-similar regime
 364 of the flow. Whenever this regime is reached, we have $\alpha_L \rightarrow \alpha$ and $\Theta \rightarrow 0$, so that:

$$\text{Self-similar regime :} \quad F_0 = \frac{d_{cc}}{\alpha + \sqrt{4\alpha + \alpha^2}} \quad . \quad (46)$$

365 Note that Eq. (45) is valid for both reactive and non-reactive Rayleigh–Taylor turbulence. However, its asymptotic
 366 self-similar expression (46) differs in both cases because the limits of α and Θ are not the same.

367 D. Main results

368 1. Asymptotic relation between α and γ

369 So far, we have derived an expression for the self-similar profile of \bar{c} as well as an expression for the concentration
 370 flux prefactor F_0 . With the help of these two intermediate results, we are now ready to express the integral \mathcal{I} that
 371 serves as a basis for relating α and γ .

372 To start with, we make the change of variable $z = y/(2F_0)$ in the definition (16b) of \mathcal{I} and inject the value (32) of
 373 \bar{c}_s . This yields:

$$\mathcal{I}(\alpha, \gamma, \mathbf{p}) = 12F_0 \int_{-1/2}^{1/2} \bar{c}_s(z; \gamma) (1 - \bar{c}_s(z; \gamma)) dz \quad . \quad (47)$$

374 Next, we replace the value of F_0 by its expression (46) and the value of the integral over z by the definition (36) of
 375 the length-scale ratio $\mathcal{G} = L/H$. With these substitutions, we are able to express \mathcal{I} as:

$$\mathcal{I}(\alpha, \gamma, \mathbf{p}) = \frac{2d_{cc}}{\alpha + \sqrt{4\alpha + \alpha^2}} \mathcal{G}(\gamma) \quad , \quad (48)$$

376 where \mathcal{G} is the known function of γ given by Eq. (38) and shown in Fig. 4(b).

377 Thus, we have derived an expression for \mathcal{I} that only involves α , γ and the same additional parameter d_{cc} that
 378 appears in the non-reactive relationships (10) and (11). All that remains to do is to solve Eq. (16a), it is to say $\mathcal{I} = 1$.
 379 This operation yields:

$$\alpha = \frac{(d_{cc} \mathcal{G}(\gamma))^2}{1 + d_{cc} \mathcal{G}(\gamma)} \quad . \quad (49)$$

380 Because \mathcal{G} is a decreasing function of γ , so is α . As shown in Fig. 5, the smaller γ is, the higher α is. And since small
 381 values of γ correspond to less mixing, the main conclusion that can be drawn from Eq. (49) is that the growth of the
 382 mixing zone is faster when the mixture is more heterogeneous. In other words, Eq. (49) confirms the intuitive link
 383 between growth rate and mixing that was mentioned in the introduction and that served as the main motivation for
 384 this work.

385 Another point worth mentioning is that α also depends on the anisotropy factor d_{cc} and increases with it. So, just
 386 as in non-reactive Rayleigh–Taylor turbulence, elongated structures are associated with a faster growth of the mixing
 387 zone.

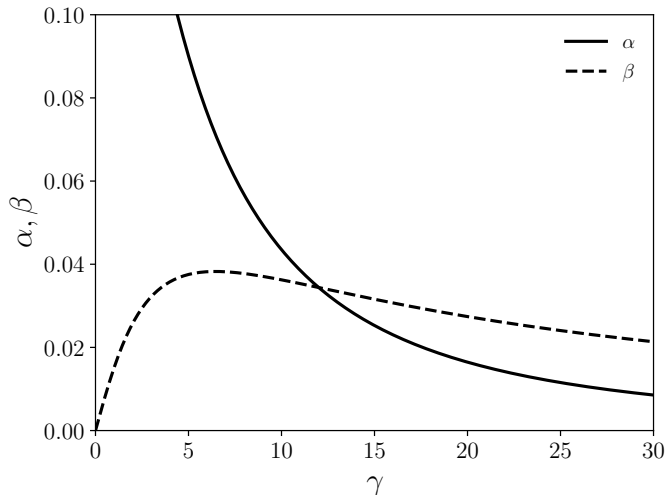


FIG. 5. Variations of α and β as a function of γ for $d_{cc} = 0.55$.

388

2. Dynamic relation between α_L , γ_L and Θ

389 Figure 3 shows an important feature of reactive Rayleigh–Taylor flows: the nearly horizontal line observed in
 390 the (α_L, Θ) graph indicates that the convergence of Θ towards its zero asymptotic value is much slower than the
 391 convergence of α_L towards α . Therefore, rather than a strict asymptotic state where Θ is equal to 0, it may be useful
 392 to account for an intermediate state where Θ is small but different from 0.

393 In this regard, most of the results derived so far can be used to analyse this intermediate state. In particular, the
 394 value of F_0 given by Eq. (45) does not depend on whether the asymptotic regime is reached or not. It remains valid
 395 even with non-zero values of Θ . The same remark applies to the truncation of the Legendre polynomial expansion
 396 of Sec. III B and by extension to Eq. (28). The only question that we need to answer is how does a finite value of
 397 Θ affect the self-similar profile \bar{c}_s deduced from Eq. (28). Without further constraints to guide us, we propose to
 398 settle for the simplest possible solution. Namely, we assume that $z(t, c)$ and F_0 remain stationary so that Eq. (30)
 399 still applies. Then, \bar{c}_s keeps its expression (32), save for one modification: the asymptotic parameter γ in Eq. (32)
 400 must be replaced by the instantaneous value of the parameter appearing in Eq. (28) as a prefactor of $c(1-c)$, it is
 401 to say by γ_L , the dynamic estimate of γ introduced in Eq. (6). Thus, replacing Eq. (46) by Eq. (45) and γ by γ_L , we
 402 deduce the following dynamic estimate of α_L :

$$\alpha_L = \frac{(d_{cc}(1-\Theta)\mathcal{G}(\gamma_L))^2}{1 + d_{cc}(1-\Theta)\mathcal{G}(\gamma_L)}. \quad (50)$$

403 The most striking property of Eq. (50) is that, even though it was derived in a reactive setting, its validity extends
 404 to non-reactive Rayleigh–Taylor flows. Indeed, the absence of reaction corresponds to the limit $\tau \rightarrow \infty$ and therefore
 405 to $\gamma_L = 0$. As a result, since $\mathcal{G}(0) = 1$, we find that:

$$\text{for } \tau \rightarrow \infty, \quad \alpha_L = \frac{(d_{cc}(1-\Theta))^2}{1 + d_{cc}(1-\Theta)}. \quad (51)$$

406 This formula is identical to Eq. (10) which was derived in [11, 12] for non-reactive Rayleigh–Taylor turbulence. Let
 407 us also mention that with $\gamma_L = 0$, the profile $\bar{c}_s(z, \gamma_L)$ given by Eq. (32) is linear, just like it was assumed in [11, 12].
 408 Thus, the reactive/non-reactive coincidence in the limit $\tau \rightarrow \infty$ not only applies to the end result (Eq. (50)) but also
 409 to the main assumptions that lead to it.

410

3. Displacement rate β

411 At the beginning of the derivation, in Sec. III A 1, we explained how the integration of Eq. (12) leads to Eq. (14),
 412 i.e. to $\beta = \gamma\alpha/12$. Combining this relation with the expression (49) of α yields the following expression of β :

$$\beta = \frac{\gamma}{12} \frac{(d_{cc}\mathcal{G}(\gamma))^2}{1 + d_{cc}\mathcal{G}(\gamma)} . \quad (52)$$

413 The most salient feature of this expression is that β is not a monotonous function of γ . It is equal to 0 for $\gamma = 0$ and
 414 decays as $3d_{cc}^2/\gamma$ for large γ . In between the two limits, β goes through a maximum. For d_{cc} on the order of 1, this
 415 maximum is reached for $\gamma = \gamma_{\max} \approx 6$ and its value verifies :

$$\beta_{\max} \approx \frac{d_{cc}}{12} \left(d_{cc} + \frac{3}{10} \right) . \quad (53)$$

416 For $d_{cc} = 0.55$, a value observed in the simulation detailed in Sec. IV, we find that $\beta_{\max} \approx 0.04$, a value obtained for
 417 $\gamma_{\max} \approx 6.5$. These properties are illustrated in Fig. 5.

418 From a physical point of view, the reason why β attains a maximum can be understood as follows. The quantity
 419 $X_c = \int (\bar{c} - \bar{c}^{(0)}) dx_3$ not only traces the displacement of the center of the mixing zone. It also corresponds to the total
 420 volume of reactant which has been burnt since initial time. Hence, β can also be seen as a measure of the increase of
 421 the consumption rate of reactants by the mixing zone. As shown by Eq. (13), this consumption rate is proportional
 422 to two factors. The first one is the width of the flame brush (L in Eq. (13)), the other the proportion of burning
 423 fluids found within this brush (Θ in Eq. (13)). These two factors vary in opposite directions with the level of mixing
 424 γ : L is proportional to α and decreases with γ while, by definition, Θ increases with γ .

425 To sum up, the dependency of β on the mixing level γ is controlled by two factors with opposing effects. The
 426 maximum predicted by Eq. (52) corresponds to the optimal consumption rate that can be achieved under these
 427 antagonizing conditions. Given the double interpretation of X_c , this maximum also corresponds to the largest ac-
 428 celeration that the center of the mixing zone can achieve. The fact that such a maximal value exists may be of
 429 importance for some applications. For instance, the transition from deflagration to detonation of Rayleigh–Taylor
 430 driven flames in type Ia supernovae is possibly influenced by the speed at which these flames travel [31].

431 To conclude on the displacement rate, we have hitherto discussed its asymptotic value β . A dynamic estimate β_L
 432 of this coefficient was introduced in Eq. (6), based on the same time scale τ_L as the one appearing in the definitions
 433 of α_L and γ_L . Because of this choice, Eq. (13) can be written in a strictly equivalent form linking α_L , β_L and γ_L :

$$\beta_L = \frac{\gamma_L}{12} \alpha_L = \frac{\gamma_L}{12} \frac{(d_{cc}(1 - \Theta)\mathcal{G}(\gamma_L))^2}{1 + d_{cc}(1 - \Theta)\mathcal{G}(\gamma_L)} . \quad (54)$$

434 Just as Eq. (50) for α_L , this prediction is valid in both reactive and non-reactive turbulence. In the latter case, we
 435 recover the trivial result:

$$\text{for } \tau \rightarrow \infty \quad , \quad \beta_L = 0 \quad . \quad (55)$$

436

IV. SIMULATIONS

437

A. Simulation setting and initial conditions

438 In order to verify the validity of the results derived in the previous section, four direct numerical simulations (DNS)
 439 and four implicit large eddy simulations (ILES) are carried out. The reason for performing ILES in addition to
 440 DNS is that the former allows to attain higher effective Reynolds numbers. This gives more leeway for exploring the
 441 thickened-wrinkled flame regime (see Fig. 2) and for attaining a state close to self-similarity. Another reason is that we
 442 are mostly interested in the evolution of the large-scale features of the flows and do not need a detailed knowledge on
 443 the evolution of small dissipative scales. These scales are of course captured by DNS. Thus, the comparison between

444 the two approaches allows to verify that the role played by these scales is not crucial for the issues at stake in this
 445 work and that no physical bias is introduced by using a numerical dissipation instead of a physical one.

446 The DNS and ILES are performed with two different codes. The DNS are done with STRATOSPEC which is a
 447 spectral code solving the reactive Boussinesq equations (1). The computational grid is a rectangular domain with
 448 regular spacing and dimensions $L_{\text{dom}} \times L_{\text{dom}} \times 2L_{\text{dom}}$ with $L_{\text{dom}} = 2\pi$. The simulations all have $2048^2 \times 4096$ cells
 449 [37].

450 The ILES are performed with TRICLADE which is a Finite-Volume solver of the compressible multimaterial Navier–
 451 Stokes equation [38, 39]. The computational grid is subdivided in three adjacent domains. The central domain is
 452 regular and has $1024^2 \times 1280$ cells. Its dimensions are $L_{\text{dom}} \times L_{\text{dom}} \times 1.25L_{\text{dom}}$ with $L_{\text{dom}} = 1$. The other domains have
 453 a geometric progression in the inhomogeneous direction. Note that, even if the code is compressible, the simulations
 454 remains in the Boussinesq limit. The Atwood number at the interface is small ($A_t = 0.025$) and the turbulent Mach
 455 number also remains small at all times.

456 For both types of simulation, a random perturbation h corrugates the interface between the two fluids. The
 457 prescribed spectrum for the perturbation takes the form :

$$P(k) = \overline{h^2} \frac{2\left(\frac{s}{2}\right)^{\frac{s+1}{2}} \lambda_0}{\Gamma\left(\frac{s+1}{2}\right) 2\pi} \left(\frac{k\lambda_0}{2\pi}\right)^s e^{-\frac{s}{2}\left(\frac{k\lambda_0}{2\pi}\right)^2} , \quad (56)$$

458 where $\overline{h^2}$ is the variance of the perturbation height, λ_0 the peak length scale of the perturbation spectrum and s the
 459 infrared exponent of the spectrum. The following parameters are set for the simulations:

$$\begin{array}{ll} \text{DNS} & : \quad s = 6 \quad , \quad \frac{\lambda_0}{L_{\text{dom}}} = 2.5 \cdot 10^{-2} \quad , \quad \frac{\sqrt{\overline{h^2}}}{L_{\text{dom}}} = 1.3 \cdot 10^{-3} \quad , \\ \text{LES} & : \quad s = 6 \quad , \quad \frac{\lambda_0}{L_{\text{dom}}} = 6 \cdot 10^{-3} \quad , \quad \frac{\sqrt{\overline{h^2}}}{L_{\text{dom}}} = 3 \cdot 10^{-3} \quad . \end{array}$$

460 The typical time of growth associated with this perturbation spectrum is given by :

$$T_{\text{RT}} = \sqrt{\frac{\lambda_0}{2\pi A_t g}} \quad , \quad (57)$$

461 This time can be compared against the reactive timescale τ , thus leading to the definition of a dimensionless parameter
 462 called initial Damköhler number Da_0 :

$$\text{Da}_0 = \frac{T_{\text{RT}}}{\tau} = \sqrt{\frac{\lambda_0}{2\pi A_t g \tau^2}} \quad . \quad (58)$$

463 For each simulation, the initial Damköhler number is modified by changing the reaction timescale τ while keeping
 464 other parameters unchanged. The value of Da_0 for each simulation is given in table I.

TABLE I. Initial Damköhler number Da_0 of simulations.

	DNS					LES			
Simulation name	NR	D1	D2	D3	D4	L1	L2	L3	L4
Da_0	0	0.8	1.6	2.5	3.3	1.0	1.6	2.1	2.6

465

466

467 The initial Damköhler number Da_0 is not expected to play a significant role in the self-similar regime. However,
 468 Da_0 plays a crucial role during the transient evolution of the flow. In particular, the value of Da_0 is the main factor
 469 that determines the delay after which the thickened-wrinkled flame regime and the self-similar regime can be reached.
 470 In this respect, two limits can be put forward. If $\text{Da}_0 \gg 1$, the reaction is much faster than the Rayleigh–Taylor
 471 instability. The laminar flame front is corrugated by the Rayleigh–Taylor instability and transitions from a flamelet
 472 to a thickened-wrinkled flame. On the other hand, when $\text{Da}_0 \ll 1$, the reaction is very slow compared to the Rayleigh–
 473 Taylor instability. As a consequence, there may be a significant time during which the reaction does not affect the
 474 evolution of the mixing zone. In that case, the flow goes transiently through the thickened flame regime before
 475 reaching the thickened-wrinkled flame regime. Examples of these different transients can be observed in Fig. 2.

476 Note that simulation NR has a Damköhler number equal to 0: the reaction time is infinite so that the simulation is
 477 non-reactive. This simulation is used as a reference against which the remaining reactive simulations can be compared.

B. Flow characteristics

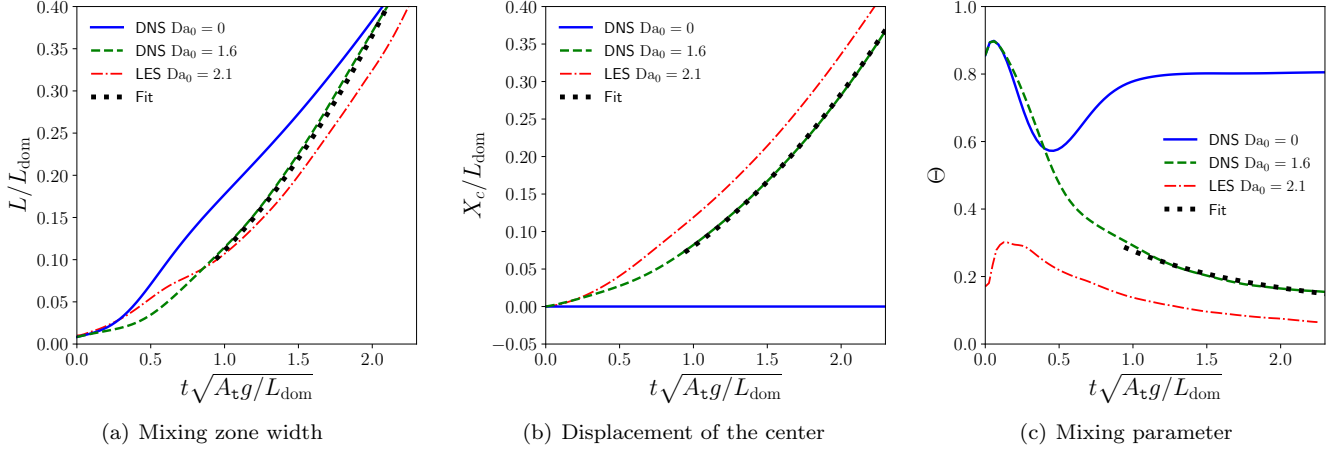


FIG. 6. Mixing zone width L , flame displacement X_c and mixing parameter for simulations NR ($\text{Da}_0 = 0$), D2 ($\text{Da}_0 = 1.6$) and L3 ($\text{Da}_0 = 2.1$). The fitted values are defined by Eq. (59) with parameters given by Eq. (60).

480 The main predictions of this work concern three quantities: the width of the mixing zone L , the displacement of
 481 its center X_c and the mixing parameter Θ (see Eq. (4)). Figure 6 illustrates how these three quantities behave for
 482 the DNS D2 ($\text{Da}_0 = 1.6$) and the LES L3 ($\text{Da}_0 = 2.1$). As a reference, the non-reactive simulation NR ($\text{Da}_0 = 0$) is
 483 also plotted in this figure. As can be seen, after a short transient, the width L and displacement X_c grow almost
 484 quadratically in time for both reactive simulations, while the mixing parameter decays almost as the inverse of time.
 485 This is confirmed by comparing their evolution with fits of the form :

$$L_{\text{fit}}(t) = \left(\sqrt{2\alpha_{\text{fit}}A_\tau g}(t - t_s) + \sqrt{L(t_s)} \right)^2, \quad X_{c,\text{fit}}(t) = \left(\sqrt{2\beta_{\text{fit}}A_\tau g}(t - t_s) + \sqrt{X_c(t_s)} \right)^2 \quad (59)$$

and
$$\Theta_{\text{fit}}(t) = \frac{\gamma_{\text{fit}}\tau}{t - t_s + \gamma_{\text{fit}}\tau/\Theta(t_s)},$$

486 where α_{fit} , β_{fit} and γ_{fit} are adjustable parameters and where t_s is a time marking the onset of self-similarity. Choosing
 487 $t_s\sqrt{A_\tau g}/L_{\text{dom}} = 1$, a best fit of the DNS with $\text{Da}_0 = 1.6$ is obtained by setting :

$$\alpha_{\text{fit}} \approx 0.037, \quad \beta_{\text{fit}} \approx 0.031 \quad \text{and} \quad \gamma_{\text{fit}} \approx 11. \quad (60)$$

488 With these values, a close agreement is observed between the actual and fitted evolutions of L , X_c and Θ . This is
 489 consistent with the expected self-similar behaviour predicted in Eq. (5). While not shown here, a similar agreement
 490 is obtained for the LES with $\text{Da}_0 = 2.1$, as well as for the remaining reactive reactions, with values of α_{fit} , β_{fit} and γ_{fit}
 491 close to those given here.

492 It is worth stressing that the value $\gamma_{\text{fit}} \approx 11$, when reported in Eq. (49) and Fig. 5, leads to values of α and β close
 493 to the fitted ones. This coherency gives a first hint as to the validity of Eq. (49). It should also be emphasized that
 494 the estimate α_{fit} is larger than the value $\alpha_{\text{nr}} = 0.02$ usually measured in non-reacting Rayleigh–Taylor simulations
 495 [4, 5, 7]. This property will be confirmed below by looking at the time evolution of α_L (see Fig. 12). Note also that
 496 the quadratic time evolution of L appears more clearly for the two reactive cases than the non-reactive one in Fig.
 497 6(a). For the latter, a longer transient is present. Figure 6(c) also shows that in the non-reactive case, Θ tends to
 498 a constant approximately equal to 0.8. As mentioned in the introduction and in Sec. II C, this is one of the major
 499 differences distinguishing reactive and non-reactive Rayleigh–Taylor turbulence.

500 This major difference is also illustrated in Fig. 7 which displays vertical cuts of the concentration and vorticity
 501 fields for the reactive DNS D2 ($\text{Da}_0 = 1.6$) and the non-reactive DNS NR ($\text{Da}_0 = 0$) at a time such that $L/L_{\text{dom}} = 0.7$.
 502 The concentration field displayed for the reactive simulation shows a domain mostly filled by pure fluids: the red
 503 and blue colors are predominant. By contrast, the non-reactive cut essentially shows intermediate colors within the
 504 mixing zone suggesting a high level of mixing.

505 Figure 7 also shows another property of reactive Rayleigh–Taylor turbulence worth mentioning. First, looking at
 506 the two cuts on the left of this figure, one can see that, in the Boussinesq limit, a non-reactive Rayleigh–Taylor

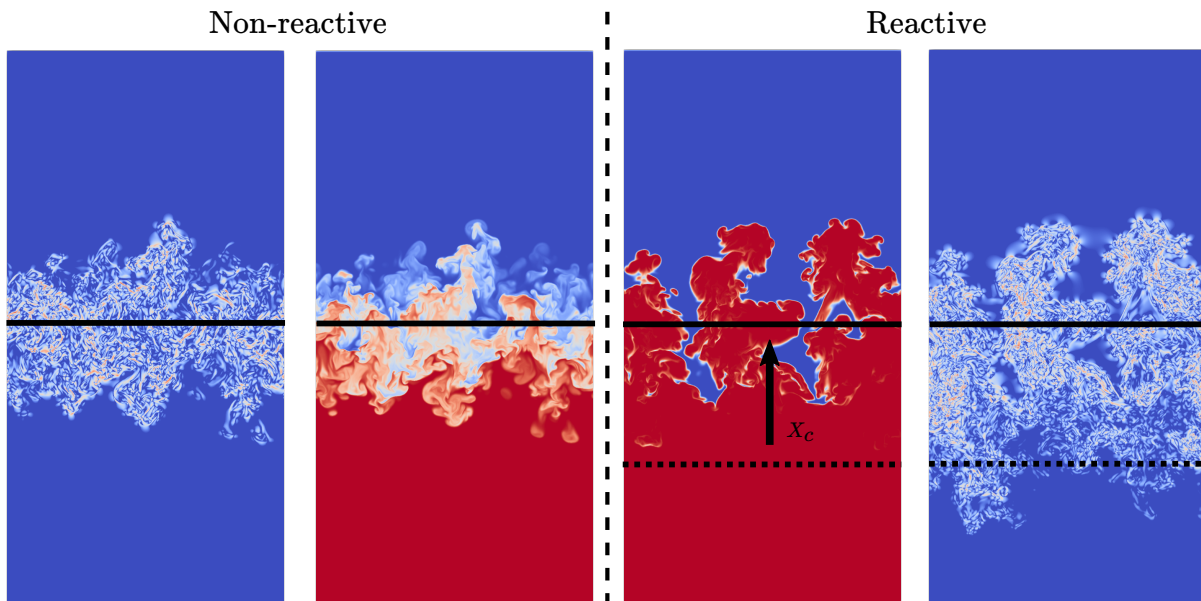


FIG. 7. Vertical slices of the concentration field and of the longitudinal vorticity magnitude $\log \omega_x^2$ for the reactive DNS D2 ($\text{Da}_0 = 1.6$) and the non-reactive DNS NR ($\text{Da}_0 = 0$) at a time such that $L/L_{\text{dom}} = 0.7$. The non-reactive DNS is shown on the left-half and the reactive DNS on the right-half of the figure. In each half, vorticity is shown on the left and concentration on the right. For the concentration field, red corresponds to $c = 1$ (light products) and blue to $c = 0$ (heavy reactants). For the vorticity field, a brighter color means a higher intensity.

507 mixing zone develops symmetrically with respect to the position of the initial interface separating the two fluids.
 508 Besides, the extent of the vorticity field roughly coincides with that of the concentration field. By contrast, the
 509 concentration and vorticity fields of the reactive case are highly asymmetrical : with respect to the layer center, their
 510 extension is greater in the direction of light products than in the direction of heavy reactants. Furthermore, one can
 511 note that the vorticity field extends below the mixing region down to the position of the initial interface and even
 512 somewhat below. To understand the origin of this observation, the interplay between vorticity production and flame
 513 displacement has to be considered. At any time, the flame is the locus of the strongest concentration gradients and
 514 hence of the strongest density gradients in the present Boussinesq flow. Due to the baroclinic torque, it means that
 515 most of the instantaneous vorticity production occurs inside the reacting zone. Then, the deposited vorticity remains
 516 attached to the fluid, and more precisely to the products, whereas the flame propagates toward the reactants. This
 517 is different from the non-reacting case, where density gradients and vorticity are both carried by the fluid, leading to
 518 persistent amplification at the same place. By contrast, in the reacting case, the vorticity deposited at any time at
 519 the instantaneous flame location decays later in the light products whereas the baroclinic production zone propagates
 520 upward toward the reactants. Would no vortex dynamics be at work, the vorticity field would be confined between
 521 the initial and the final position of the flame front. In the right half of Fig. 7, it would correspond to the red region
 522 of products above the dashed line. However, this trailing field is not passive and turbulent motions may entrain some
 523 fluid with its vortical content below the initial flame location as seen in Fig. 7. This is also seen in Fig. 1 which shows
 524 a volume rendering of the concentration field.

526

C. Verification of the assumptions

527 To derive the results presented in Sec. IIID, we made two major assumptions. First, we assumed that the flux
 528 and variance of the concentration can be approximated by a truncated Legendre approximation. Second, we assumed
 529 that the growing mode of the buoyancy production term is large compared to the other ones and is dominant in the
 530 expressions of the concentration flux and variance. The relevance of these two assumptions is assessed below.

531 Besides, we also check whether the anisotropy coefficient d_{cc} remains constant and close to the same value in the
 532 different simulations. This condition is not a requirement for the derivation of Eqs. (49)-(50) and (52)-(54). However,
 533 if it is not verified, d_{cc} cannot be regarded as a fixed parameter and some additional considerations would be needed
 534 to make full sense of Eqs. (49)-(50) and (52)-(54).

1. Spatial profiles of the flux and variance of concentration

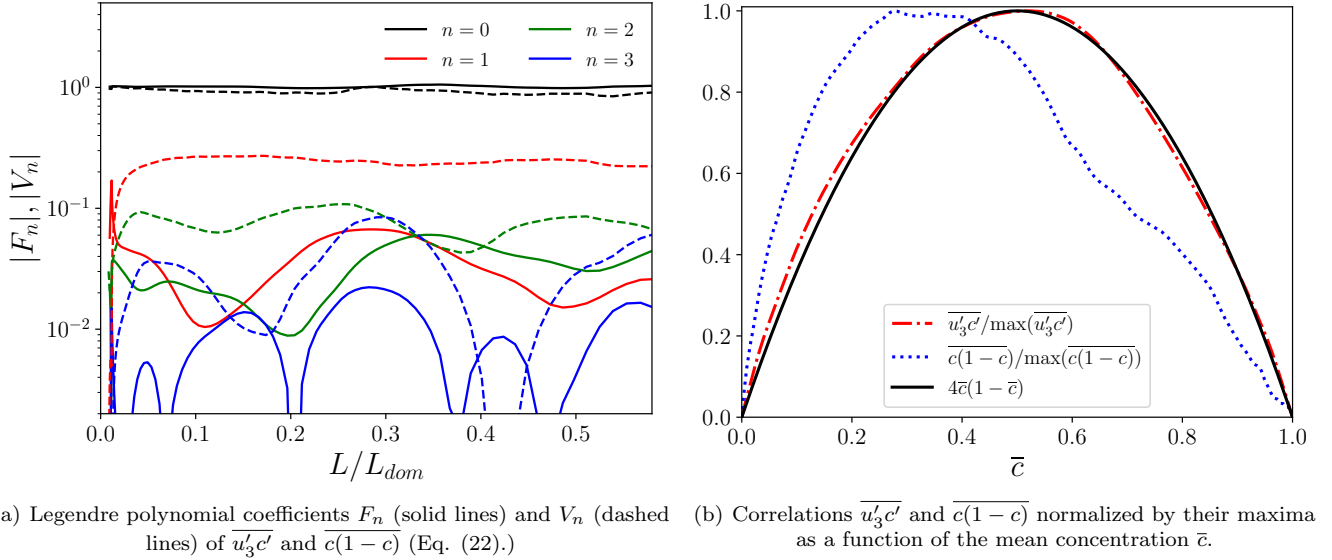


FIG. 8. Dependency of the spatial profiles of $\overline{u'_3 c'}$ and $\overline{c(1-c)}$ on the mean concentration \bar{c} . Results taken from simulation D4, at the time for which $L/L_{\text{dom}} = 0.2$ for (b).

536 The first pivotal hypothesis made in this work is expressed by Eq. (25). It consists in assuming that the correlations
 537 $\overline{u'_3 c'}$ and $\overline{c(1-c)} = \overline{c(1-c)} - \overline{c'^2}$ are proportional to $\bar{c}(1-\bar{c})$ and to a time-dependent constant. This assumption
 538 can be understood as the result of the truncation of the Legendre polynomial expansion (22) and may be justified
 539 provided the higher-order coefficients of this expansion are much smaller than its zero-*th* order (Eq. (24)).

540 To verify these elements, we plot in Fig. 8(a) the first three Legendre polynomial coefficients of $\overline{u'_3 c'}$ and $\overline{c(1-c)}$
 541 for simulation D4 as a function of time. These coefficients are computed according to the formulas:

$$F_n(t) = \int_0^1 \frac{\overline{u'_3 c'}}{4 \max(\overline{u'_3 c'})} \bar{c}(1-\bar{c}) \tilde{P}_n(\bar{c}) d\bar{c} \quad \text{and} \quad V_n(t) = \int_0^1 \frac{\overline{c(1-c)}}{4 \max(\overline{c(1-c)})} \bar{c}(1-\bar{c}) \tilde{P}_n(\bar{c}) d\bar{c} \quad . \quad (61)$$

542 The first observation is that F_0 and V_0 are indeed much larger than their respective higher order coefficients F_i and
 543 V_i with $i \in \{1, 2, 3\}$. This is coherent with Eq. (24) and with the possibility of truncating expansion (22). A second
 544 observation worth mentioning is that the first 3 coefficients of the expansion vary little in time. This implies that
 545 almost from the start of the simulation, way before the self-similar turbulent regime has begun, the profiles of $\overline{u'_3 c'}$ and
 546 $\overline{c(1-c)}$ expressed as a function of \bar{c} have already almost settled to their asymptotic shapes. The larger fluctuations
 547 observed for F_3 and V_3 might be assigned to the statistical fluctuations that inevitably deform correlation profiles.

548 To provide a more direct verification of Eq. (25), we display in figure 8(b) the correlations $\overline{u'_3 c'}$ and $\overline{c(1-c)}$
 549 normalized by their maxima as a function of \bar{c} . These profiles are shown for simulation D4 at the time for which
 550 $L/L_{\text{dom}} = 0.2$. For $\overline{u'_3 c'}$, a close agreement is observed with the parabola $4\bar{c}(1-\bar{c})$, as expected from Eq. (25).
 551 However, for $\overline{c(1-c)}$, a non-negligible asymmetry of the normalized shape is observed. Its peak is indeed reached for
 552 $\bar{c} \approx 0.35$ instead of 0.5. This asymmetry comes from the coefficient V_1 of the Legendre expansion and, even though
 553 it appears significant, its effects on the results presented so far are not. To check it, the derivation of Sec. III has
 554 been performed again keeping the contribution of V_1 . While this modified derivation is not detailed here, we found
 555 no important changes to the self-similar concentration profile \bar{c}_s nor to the eventual dependency of α and β on γ ,
 556 provided V_1/V_0 remains small as is the case in our simulations. In particular, with the ratio V_1/V_0 displayed in Fig.
 557 8(a), the formula accounting for V_0 and V_1 only differ by a few percents from Eqs. (49) and (52) which only account
 558 for V_0 .

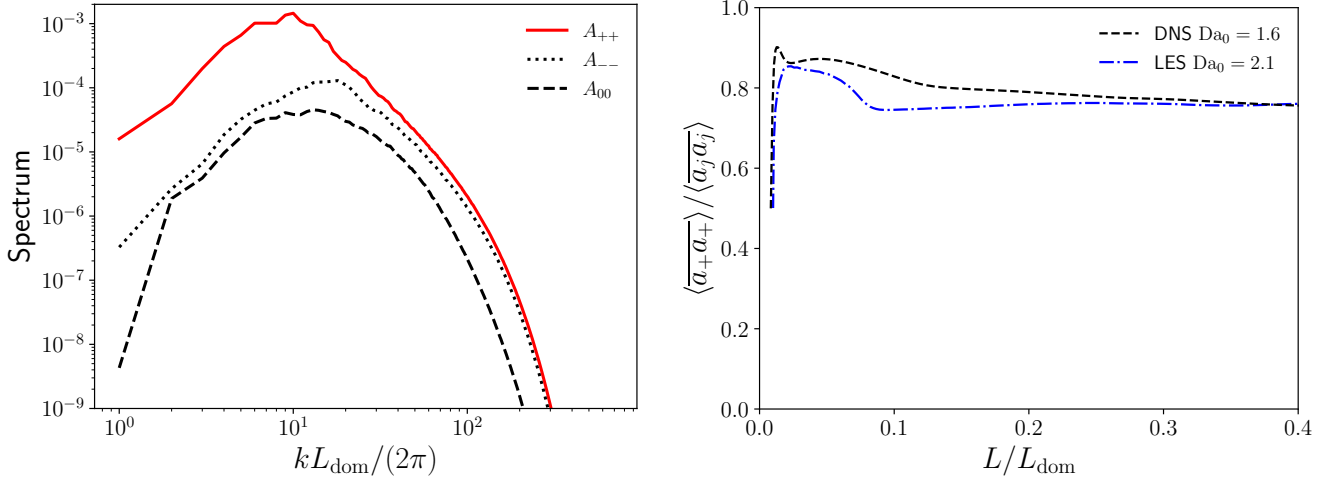
559 Thus, as whole, the results displayed in Figs. 8(a) and 8(b) appear compatible with the assumption given in Sec.
 560 IIIB.

561

2. Predominance of the growing mode

562 The second major hypothesis of this work is described in Sec. III C and consists in assuming that, among the three
 563 eigenmodes of the homogenized linear buoyancy production term, the growing one, a_+ is much larger than the other
 564 two a_- and a_0 . This condition is expressed by Eq. (40).

565 To verify this assumption, we begin by comparing the three-dimensional spectra A_{++} , A_{00} and A_{--} of each of
 566 these modes. Figure 9(a) shows this comparison for simulation D4 at a time such that $L/L_{\text{dom}} = 0.14$. It can be seen
 567 that A_{++} is indeed much larger than A_{00} and A_{--} at large and energetic scales. A more direct verification of Eq.
 568 (40) is obtained by plotting the ratio $\langle \overline{a_+^2} \rangle / \langle \overline{a_j a_j} \rangle$ as a function of time. This is done in Fig. 9(b) for simulations D2
 569 and L3. It can be seen that $\langle \overline{a_+^2} \rangle$ throughout the simulations represents more than 75 % of the sum $\langle \overline{a_j a_j} \rangle$ which
 570 measures the total energy, i.e. the sum of the kinetic and potential energies. Overall, the results displayed in Figs.
 571 9(a) and 9(b) are consistent with assumption (40).



(a) Spectra of the homogeneous eigenmodes a_+ , a_- and a_0 for simulation D4 at a time such that $L/L_{\text{dom}} = 0.14$.

(b) Relative contribution of the growing eigenmode a_+ to the total energy for simulations D2 and L3.

FIG. 9. Illustration of the predominance of the growing eigenmode.

572

3. Anisotropy parameter d_{cc}

573 Even though it is not required for their derivations, we still interpreted and manipulated relations (49)-(50) and (52)-
 574 (54) with the implicit expectation that d_{cc} attains a constant value independent from initial conditions. Otherwise,
 575 relations (49)-(50) and (52)-(54) would still be valid but unknown dependencies would remain hidden in the value of
 576 d_{cc} . To verify that this is not the case, we invert relation (45) and express d_{cc} as:

$$d_{cc} = \frac{F_0}{1 - \Theta} \left(\alpha_L + \sqrt{4\alpha_L + \alpha_L^2} \right) \quad . \quad (62)$$

577 This expression is plotted as function of time for the DNS and LES simulations in Fig. 10. It can be seen that
 578 d_{cc} indeed reaches a constant value and that this value varies by less than 10% in the different simulations. More
 579 precisely, we observe that for $L/L_{\text{dom}} > 0.2$, we have:

$$d_{cc} \approx 0.55 \pm 10\% \quad . \quad (63)$$

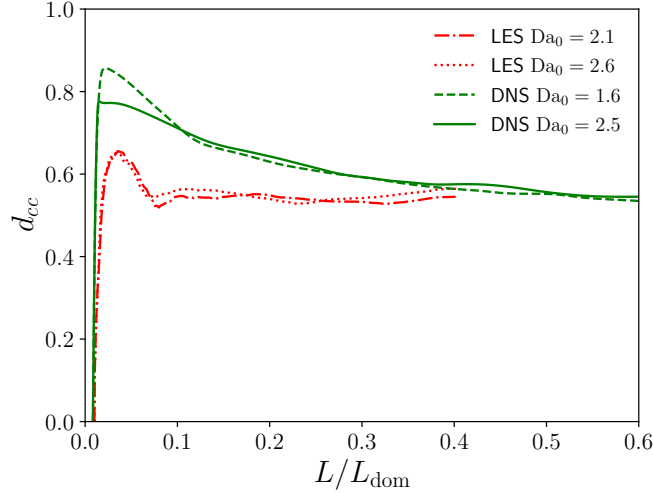


FIG. 10. Evolution of d_{cc} given by formula (62) as a function of L/L_{dom} for the DNS and LES simulations.

580

D. Main predictions

581

1. Mean concentration profile

582 Assumptions (25) and (40) lead to several predictions and in particular to the derivation of the analytic formula
 583 (32) giving the mean concentration profile as a function of the reduced coordinate $z = x_3/(2F_0L)$. This expression
 584 is valid at asymptotically large times. However, for the simulations performed in this work, the transient preceding
 585 the self-similar regime induces an offset of the profiles that survives until the simulations end. This offset prevents a
 586 direct comparison of Eq. (32) with simulation results.

587 To circumvent this difficulty, we propose to account for the transient part of the simulation in the expression of
 588 z . Namely, in the preceding subsection, we observed in Figs. 8(a) and 9(b) that assumptions (25) and (40) are valid
 589 almost from the start of the simulations. This means that the unstationary equation (28) giving the evolution of z as a
 590 function of time and \bar{c} is also valid at these early times. As a result, the transient evolution of z can be computed from
 591 Eq. (28). This can be done by using the method of characteristics, assuming that the viscous terms are negligible.
 592 This yields:

$$z(t^*, \bar{c}) = z_{\text{off}}(t^*, \bar{c}) + C_z(t^*)z_{\text{cent}}(t^*, \bar{c}) \quad (64a)$$

$$\text{with } z_{\text{off}}(t^*, \bar{c}) = z_{\text{init}} \left(\frac{\bar{c}e^{-\Delta\Gamma(0,t^*)/2}}{1 - c + ce^{-\Delta\Gamma(0,t^*)/2}} \right) \frac{F_{0,\text{init}}}{F_0(t^*)} e^{-t^*} \quad , \quad (64b)$$

$$z_{\text{cent}}(t^*, \bar{c}) = -\frac{1}{2C_z(t^*)} \int_0^{t^*} e^{-(t^*-s)} \frac{F_0(s)}{F_0(t^*)} \frac{\bar{c}e^{-\Delta\Gamma(s,t^*)/2} - (1 - \bar{c})}{\bar{c}e^{-\Delta\Gamma(s,t^*)/2} + (1 - \bar{c})} ds \quad , \quad (64c)$$

$$C_z(t^*) = \int_0^{t^*} e^{-(t^*-s)} \frac{F_0(s)}{F_0(t^*)} ds \quad (64d)$$

$$\text{and } t^* = \int_0^t \frac{dt'}{\tau_L(t')} \quad , \quad \Delta\Gamma(s, t^*) = \int_s^{t^*} \gamma_L(t') dt' \quad . \quad (64e)$$

593 The different terms of these expressions can be computed using the values of F_0 and γ_L extracted from the simulations.
 594 This allows to separate the contribution of the offset due to the initial condition, z_{off} , from the contribution converging
 595 to the self-similar solution (31) in a symmetric fashion at large times, z_{cent} .

596 Figure 11 shows the value of \bar{c} as a function of z_{cent} for simulation D3 at a time for which $L/L_{\text{dom}} = 0.4$. This
 597 simulation result is compared against the expression of \bar{c}_s given by Eq. (32) with $\gamma = 9$ set to the measured value of
 598 γ_L at $L/L_{\text{dom}} = 0.4$. A good agreement is observed between prediction and simulation. The most salient difference
 599 is observed at the foot of the concentration profile. In the simulation, a small overshoot extends beyond the limit
 600 $z = 0.5$, which is not predicted by Eq. (32). Similar observations are made at different times and also for the other
 601 simulations, whether they are DNS or LES.

602 To insist on the difference between the reactive and non-reactive cases, we also plotted in Fig. 11 the profile obtained
 603 for the non-reactive Rayleigh–Taylor simulation NR. It can be seen that the non-reactive profile remains mostly
 604 symmetric and varies almost linearly for $z_{\text{cent}} \in [-0.5, 0.5]$. By contrast, the reactive profile is highly asymmetric and
 605 varies rapidly close to $z_{\text{cent}} = 0.5$. Note that deviations from linearity appear close to the edges of the non-reactive
 606 zone.

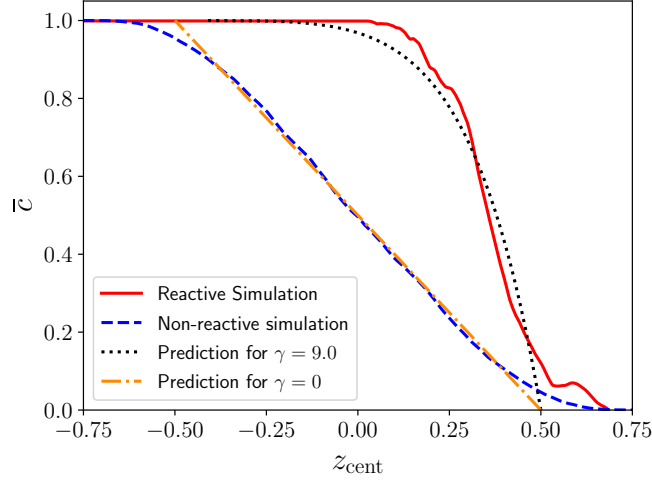


FIG. 11. Mean concentration profile as a function of the reduced coordinate z_{cent} (Eq. (64)). Comparison between the reactive DNS D3, the non-reactive DNS NR and the analytical prediction Eq. (32) at a time such that $L/L_{\text{dom}} = 0.4$. For the non-reactive prediction, the value $\gamma = 0$ is used in Eq. (32) and for the reactive one, the value $\gamma = 9$ measured in the simulation is used.

607

2. Growth and displacement rates, α and β

608 In Sec. IIID we derived formulas relating the asymptotic parameters α , β and γ as well as formulas relating
 609 instantaneous estimates of these parameters denoted by α_L , β_L and γ_L . In simulations, only the latter quantities can
 610 be extracted so that the main predictions that can be checked are Eqs. (50) and (54).

611 A first way of assessing these predictions is by injecting into the right-hand side of Eqs. (50) and (54) the instan-
 612 taneous values of d_{cc} , Θ and γ_L computed in the simulations and by comparing the outcome against the values of
 613 α_L and β_L , also computed in the simulations by using their definitions (6). This comparison is shown in Fig. 12 for
 614 simulations D2 and L4. A good agreement is obtained between simulation and prediction. This agreement occurs
 615 early in the simulation, before the onset of the self-similar regime. This is coherent with the previous observations
 616 according to which assumptions (25) and (40) are verified at early times (see Fig. 8(a) and 9). Similar outcomes are
 617 observed for the remaining simulations. Another way of verifying Eqs. (50) and (54) is by focusing on the late times
 618 of the simulations, when the flow is close to its self-similar state and still far from being confined. This “self-similar”
 619 interval of time is observed when $0.1 < L/L_{\text{dom}} < 0.4$ for LES and when $0.2 < L/L_{\text{dom}} < 0.4$ for DNS. For these
 620 intervals of time, d_{cc} is approximately constant and equal to its asymptotic value of 0.55 (see Fig. 10 and Eq. (63)).
 621 Then, Eqs. (50) and (54) can be assessed by enforcing this constant value in their right-hand sides.

622 However, even with this specification, Eqs. (50) and (54) remain hybrid relations that combine two different metrics
 623 of the mixing level : Θ and γ_L . And even though Θ tends to 0, its influence lingers. To cast this influence aside and
 624 isolate the dependency on γ_L , we therefore propose to introduce the following modified values of α_L and β_L :

$$\alpha_L^* = \frac{(s_\alpha/(1-\Theta))^2}{1+s_\alpha/(1-\Theta)} \quad \text{and} \quad \beta_L^* = \frac{(s_\beta/(1-\Theta))^2}{\gamma_L/12+s_\beta/(1-\Theta)} \quad (65)$$

$$\text{with} \quad s_\alpha = \frac{\alpha_L + \sqrt{4\alpha_L + \alpha_L^2}}{2} \quad \text{and} \quad s_\beta = \frac{\beta_L + \sqrt{\gamma_L\beta_L/3 + \beta_L^2}}{2} .$$

626 When $\Theta = 0$, one has $\alpha_L^* = \alpha_L$ and $\beta_L^* = \beta_L$ so that the two sets of quantities carry the same asymptotic information.
 627 However, they differ at intermediate times when $\Theta \neq 0$. The interest of defining α_L^* and β_L^* is the following. Injecting
 628 Eqs. (50) and (54) into these expressions, we find the following prediction for the values of α_L^* and β_L^* :

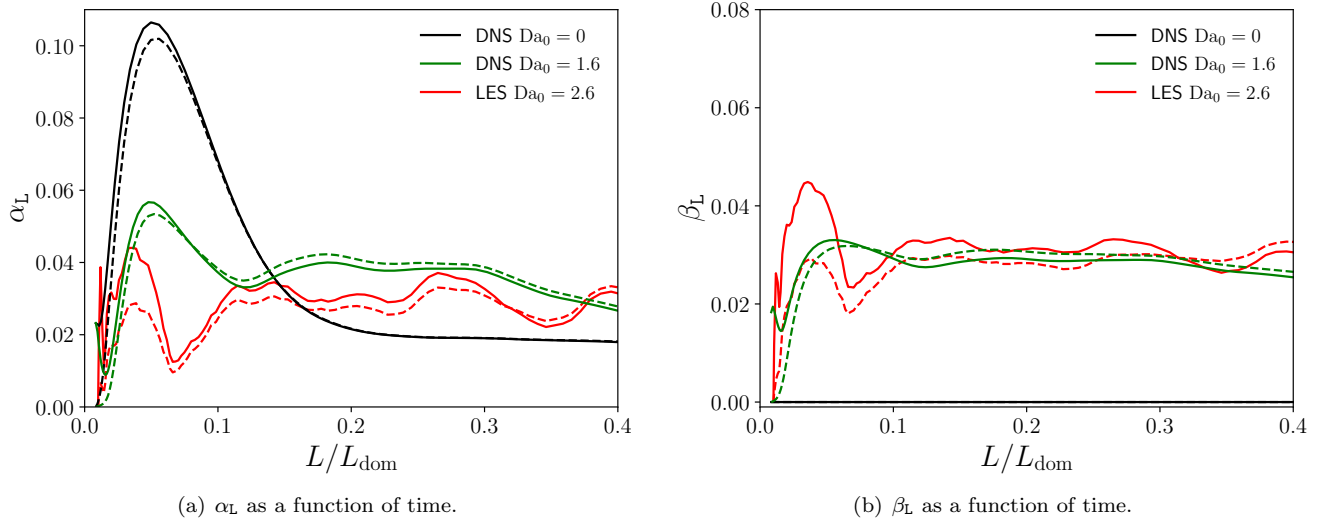


FIG. 12. Time evolution of α_L and β_L for simulations D2 and L4. Comparison between the instantaneous estimates of α_L and β_L (Eq. (6)) and their theoretical predictions (Eqs. (50) and (54)). **Plain lines: simulations. Dashed lines: predictions.**

$$\alpha_L^* = \frac{(d_{cc}\mathcal{G}(\gamma_L))^2}{1 + d_{cc}\mathcal{G}(\gamma_L)} \quad \text{and} \quad \beta_L^* = \frac{\gamma_L (d_{cc}\mathcal{G}(\gamma_L))^2}{12(1 + d_{cc}\mathcal{G}(\gamma_L))} . \quad (66)$$

Thus, even when $\Theta \neq 0$, the predicted values of α_L^* and β_L^* only depend on γ_L . These predicted values can thus be compared more easily against simulation results.

This comparison is shown in Fig. 13. Simulation results are displayed for the “self-similar” interval of time mentioned above and correspond to a direct evaluation of α_L^* and β_L^* as given by Eq. (65). The theoretical curve shown as a black line corresponds to Eq. (66) with $d_{cc} = 0.55$. As can be seen, the simulation points align along the theoretical curve for values of γ_L ranging from 8 to 20, the largest differences being on the order of 15%. It is worth highlighting that, for this range of γ_L , α_L^* has ample variations spreading in between 0.015 and 0.06. By contrast, β_L^* only varies between 0.027 and 0.042.

Another point worth mentioning is that, as time increases, the simulation points, whether DNS or LES, converge towards a small region centered around :

$$\gamma_\infty \approx 12 \quad , \quad \alpha_\infty \approx 0.037 \quad , \quad \beta_\infty \approx 0.037 \quad . \quad (67)$$

These values are coherent with the fitted parameters (60).

The reason why a convergence occurs towards these values cannot be answered by the analysis presented in this work. Nor can it be said whether this convergence is universal or not. Concerning this last point, we recall that the asymptotic value of α_{nr} obtained in non-reactive Rayleigh–Taylor turbulence is predicted to be independent from large-scale initial conditions [17] : the latter are superseded by non-linear back-scattering processes and are eventually forgotten. To determine whether a similar conclusion applies for the reactive case, an analysis of the large-scale part of the turbulent spectra of concentration and velocity would be required.

V. CONCLUSIONS

In this work, we studied the relation between the mixing level and the growth of a reactive Rayleigh–Taylor mixing zone. We showed that with less mixing, the width of the mixing zone grows faster. This conclusion is qualitatively the same as the one obtained in the non-reactive case. We also showed that an optimal value of the mixing level exists that maximizes the displacement of the mixing zone center, also congruent with the consumption rate of the reactants. As a result, the flame speed cannot exceed a maximal value determined by the directional anisotropy of turbulent structures.

Quantitative formula relating the growth and displacement rates, α and β , to the mixing level prefactor γ were derived. In doing so, we also obtained a prediction for the shape of the mean concentration profile. The latter is far from trivial: it is asymmetric and displays two distinct zones, a fast varying one close to reactants and a slow varying

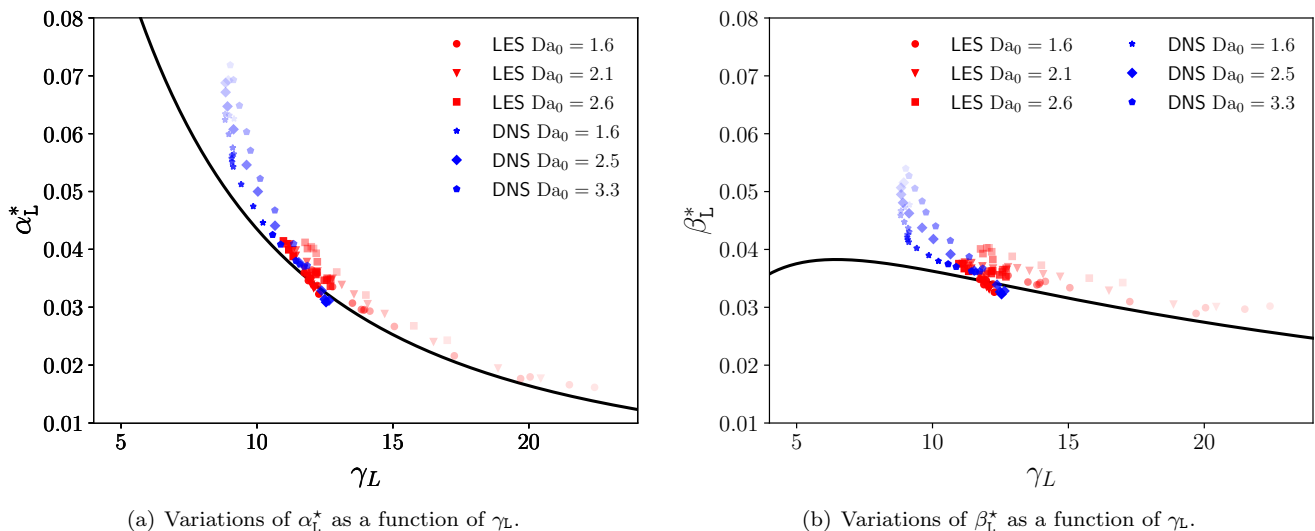


FIG. 13. Variations of α_L^* and β_L^* defined by Eq. (65) as a function of γ_L . Comparison between simulations results (colored points) and the theoretical prediction (66) with $d_{cc} = 0.55$ (black lines). The simulation points are plotted at different times such that $0.3 < H/L_{\text{dom}} < 0.75$ for DNS and $0.2 < H/L_{\text{dom}} < 0.75$ for LES. The timeline of the simulation is indicated by the opacity of the symbols: the more opaque, the further in time.

656 trailing edge. All of these predictions were assessed using DNS and LES with a resolution high enough to reach states
 657 close to the self-similar regime but still unconfined.

658 As a perspective, we note that, despite their intrinsic interest, the formula relating α , β and γ do not allow to
 659 determine a particular value of these coefficients. Some additional information is required. It could possibly be
 660 obtained by studying the very large scales of the flow, as was done in the non-reactive case [17]. This will be the
 661 object of a future work. As another perspective, we would like to stress that the dominant mode assumption used in
 662 this work not only impacts the concentration field but also the velocity field. Thus, additional relation can in principle
 663 be obtained to link some properties of the velocity field to the level of mixing. Some of these aspects are discussed in
 664 App. B. In particular, the value of the constant appearing in turbulent flame speed models is shown to depend on
 665 the mixing parameter prefactor γ .

-
- 666 [1] D. H. Sharp. An overview of Rayleigh-Taylor instability. *Physica D*, 12:3–18, 1984.
 667 [2] H.-J. Kull. Theory of the Rayleigh-Taylor instability. *Phys. Rep.*, 206(5):197–325, 1991.
 668 [3] G. Boffetta and A. Mazzino. Incompressible Rayleigh-Taylor turbulence. *Ann. Rev. Fluid Mech.*, 49:119–143, 2017.
 669 [4] Y. Zhou. Rayleigh–Taylor and Richtmyer–Meshkov instability induced flow, turbulence, and mixing. I. *Phys. Rep.*,
 670 720-722:1–136, 2017.
 671 [5] Y. Zhou. Rayleigh–Taylor and Richtmyer–Meshkov instability induced flow, turbulence, and mixing. II. *Phys. Rep.*,
 672 723-725:1–160, 2017.
 673 [6] D. L. Youngs. Numerical simulation of turbulent mixing by Rayleigh-Taylor instability. *Physica D*, 12(1-3):32–44, 1984.
 674 [7] G. Dimonte, D.L. Youngs, A. Dimits, S. Weber, M. Marinak, S. Wunsch, C. Garasi, A. Robinson, M.J. Andrews,
 675 P. Ramaprabhu, A.C. Calder, B. Fryxell, J. Biello, L. Dursi, P. MacNeice, K. Olson, P. Ricker, R. Rosner, F. Timmes,
 676 H. Tufo, Y.-N. Young, and M. Zingale. A comparative study of the turbulent Rayleigh-Taylor instability using high-
 677 resolution three-dimensional numerical simulations: The Alpha-Group collaboration. *Phys. Fluids*, 16(5):1668–1693, 2004.
 678 [8] P. Ramaprabhu and M. J. Andrews. Experimental investigation of Rayleigh–Taylor mixing at small Atwood numbers. *J.*
 679 *Fluid. Mech.*, 502:233–271, 2004.
 680 [9] G. Dimonte. Dependence of turbulent Rayleigh-Taylor instability on initial perturbations. *Phys. Rev. E*, 69:056305, 2004.
 681 [10] P. Ramaprabhu, G. Dimonte, and M.J. Andrews. A numerical study of the influence of initial perturbations on the
 682 turbulent Rayleigh-Taylor instability. *J. Fluid Mech.*, 536:285–319, 2005.
 683 [11] B.-J. Gréa. The rapid acceleration model and growth rate of a turbulent mixing zone induced by Rayleigh-Taylor instability.
 684 *Phys. Fluids*, 25:015118, 2013.
 685 [12] O. Soulard, J. Griffond, and B.-J. Gréa. Influence of the mixing parameter on the second order moments of velocity and
 686 concentration in Rayleigh-Taylor turbulence. *Phys. Fluids*, 28(6):065107, 2016.

- 687 [13] W.H. Cabot and A.W. Cook. Reynolds number effects on Rayleigh-Taylor instability with possible implications for type
688 Ia supernovae. *Nat. Phys.*, 2:562, 2006.
- 689 [14] O. Poujade and M. Peybernes. Growth rate of Rayleigh-Taylor turbulent mixing layers with the foliation approach. *Phys.*
690 *Rev. E*, 81:016316, 2010.
- 691 [15] D. Livescu, T. Wei, and M. R. Petersen. Direct numerical simulations of Rayleigh–Taylor instability. *J. Phys.: Conf. Ser.*,
692 318:082007, 2011.
- 693 [16] D.L. Youngs. The density ratio dependence of self-similar Rayleigh–Taylor mixing. *Phil. Trans. R. Soc. A*, 371:20120173,
694 2013.
- 695 [17] O. Souldard, J. Griffond, and B.-J. Gréa. Large-scale analysis of unconfined self-similar Rayleigh-Taylor turbulence. *Phys.*
696 *Fluids*, 27:095103, 2015.
- 697 [18] C. Almarcha, P. Trevelyan, P. Grosfils, and A. De Wit. Chemically driven hydrodynamic instabilities. *Phys. Rev. Lett.*,
698 104(4):044501, 2010.
- 699 [19] C. Almarcha, Y. R’Honi, Y. De Decker, P.M.J. Trevelyan, K. Eckert, and A. De Wit. Convective mixing induced by
700 acid-base reactions. *J. Phys. Chem. B*, pages 9739–9744, 2011.
- 701 [20] A. De Wit. Miscible density fingering of chemical fronts in porous media: Nonlinear simulations. *Phys. Fluids*, 16(1):163–
702 175, 2004.
- 703 [21] M. De Paoli, V. Giurgiu, F. Zonta, and A. Soldati. Universal behavior of scalar dissipation rate in confined porous media.
704 *Phys. Rev. Fluids*, 4(10):101501, 2019.
- 705 [22] P. Trevelyan, C. Almarcha, and A. De Wit. Buoyancy-driven instabilities around miscible $A + B \rightarrow C$ reaction fronts: a
706 general classification. *Phys. Rev. E*, 91(2):023001, 2015.
- 707 [23] A. De Wit. Chemo-hydrodynamic patterns and instabilities. *Ann. Rev. Fluid Mech.*, 52:531–555, 2020.
- 708 [24] N. Attal and P. Ramaprabhu. The stability of reacting single-mode Rayleigh–Taylor flames. *Physica D*, 404:132353, 2020.
- 709 [25] B. E. Morgan, B.J. Olson, W.J. Black, and J.A. McFarland. Large-eddy simulation and Reynolds-averaged Navier-Stokes
710 modeling of a reacting Rayleigh-Taylor mixing layer in a spherical geometry. *Phys. Rev. E*, 98:033111, 2018.
- 711 [26] B. E. Morgan. Simulation and Reynolds-averaged Navier-Stokes modeling of a three-component Rayleigh-Taylor mixing
712 problem with thermonuclear burn. *Phys. Rev. E*, 105(4):045104, 2022.
- 713 [27] A. M. Khokhlov. Propagation of turbulent flames in supernovae. *ApJ*, 449:695, 1995.
- 714 [28] M. Zingale, S. E. Woosley, C. A. Rendleman, M. S. Day, and J. B. Bell. Three-dimensional numerical simulations of
715 Rayleigh-Taylor unstable flames in type Ia supernovae. *The Astrophysical Journal*, 632(2):1021, 2005.
- 716 [29] N. Vladimirova. Model flames in the boussinesq limit: rising bubbles. *Comb. Theor. Mod.*, 11(3):377–400, 2006.
- 717 [30] M. Chertkov, V. Lebedev, and N. Vladimirova. Reactive Rayleigh-Taylor turbulence. *J. Fluid Mech.*, 633:1–16, 2009.
- 718 [31] E.P. Hicks and R. Rosner. Gravitationally unstable flames: Rayleigh–Taylor stretching versus turbulent wrinkling. *ApJ*,
719 771(2):135, 2013.
- 720 [32] E.P. Hicks. Rayleigh–Taylor unstable flames—fast or faster? *ApJ*, 803(2):72, 2015.
- 721 [33] E.P. Hicks. Rayleigh-Taylor unstable flames at higher reynolds number. *MNRAS*, 489:36–51, 2019.
- 722 [34] M. Liu and E.P. Hicks. Rayleigh–Taylor unstable flames: the coupled effect of multiple perturbations. *arXiv*,
723 arXiv:2309.15046, 2023.
- 724 [35] DT Casey, VA Smalyuk, RE Tipton, JE Pino, GP Grim, BA Remington, DP Rowley, SV Weber, M Barrios, LR Benedetti,
725 et al. Development of the CD Symcap platform to study gas-shell mix in implsions at the National Ignition Facility.
726 *Phys. Plasmas*, 21(9), 2014.
- 727 [36] R. Borghi and M. Destriau. *La combustion et les flammes*. Éditions Technip, 1995.
- 728 [37] A. Briard, L. Gostiaux, and B.-J. Gréa. The turbulent faraday instability in miscible fluids. *J. Fluid Mech.*, 883:A57, 2020.
- 729 [38] S. Shanmuganathan, D.L. Youngs, J. Griffond, B. Thornber, and R.J.R. Williams. Accuracy of high-order density-based
730 compressible methods in low Mach vortical flows. *Int. J. Numer. Meth. Fluids*, page DOI: 10.1002/flid.3853, 2013.
- 731 [39] B. Thornber, J. Griffond, O. Poujade, N. Attal, H. Varshochi, P. Bigdelou, P. Ramaprabhu, B. Olson, J. Greenough,
732 Y. Zhou, et al. Late-time growth rate, mixing, and anisotropy in the multimode narrowband Richtmyer-Meshkov instability:
733 The θ -group collaboration. *Phys. Fluids*, 29(10):105107, 2017.
- 734 [40] G. Damköhler. Der einfluss der turbulenz auf die flammengeschwindigkeit in gasgemischen. *Zeitschrift für Elektrochemie*
735 *und angewandte physikalische Chemie*, 46(11):601–626, 1940.

736 Appendix A: About the definitions of α and L

737 From the start of this study, we focused on the particular definition of L given by Eq. (4): $L = 6 \int \bar{c}(1 - \bar{c}) dx_3$. This
738 definition involves a numerical parameter, 6, and one may wonder why this specific value is important. This question
739 is all the more pressing than α is directly proportional to this prefactor and that establishing a relation between α
740 and γ would be pointless if α was defined up to an arbitrary multiplicative constant.

741 What constrains α in our derivation is the eigenmode analysis detailed in this very section. For the definition of
742 the eigenmodes a_+ , a_- and a_0 to be valid and for relations (44) and (45) to hold, the buoyancy production terms
743 must emulate those of a homogeneous flow. In particular, we must have:

$$\langle \overline{u'_3 c'} \partial_3 \bar{c} \rangle = -\frac{1}{L} \langle \overline{u'_3 c'} \rangle \quad , \quad (\text{A1})$$

744 with a similar relationship for $\overline{c'^2}$. So let us assume temporarily that $L = \delta \int \bar{c}(1 - \bar{c})dx_3$ with δ an unknown constant.
 745 Then, using the truncated Legendre expansion (25) of $\overline{u'_3 c'}$ and knowing that $\partial_3 \bar{c} < 0$, we find that:

$$\langle \overline{u'_3 c' \partial_3 \bar{c}} \rangle = \frac{F_0 V_L}{L} \int \bar{c}(1 - \bar{c}) \partial_3 \bar{c} dx_3 = -\frac{F_0 V_L}{L} \int_0^1 \bar{c}(1 - \bar{c}) d\bar{c} = -\frac{F_0 V_L}{6L} \quad , \quad (\text{A2a})$$

$$\text{and} \quad \frac{1}{L} \langle \overline{u'_3 c'} \rangle = \frac{F_0 V_L}{L} \frac{\int \bar{c}(1 - \bar{c}) dx_3}{L} = \frac{F_0 V_L}{\delta L} \quad . \quad (\text{A2b})$$

746 Thus, to satisfy Eq. (A1), we must have $\delta = 6$. This removes any ambiguity in the definitions of α and L used in this
 747 work: they are necessarily associated with the numerical prefactor 6 appearing in the definition (4) of L .

748

Appendix B: Energy budget and flame speed

749 In the main text, our analysis has focused almost entirely on the properties of the concentration field and of its
 750 mean value \bar{c} . This restricted scope was indeed sufficient to achieve our main objective, i.e. deriving Eqs. (49)-(50)
 751 and (52)-(54) which link α and β to γ . Still, further interesting information can be gathered by looking at other
 752 quantities and in particular at the velocity field and at the turbulent kinetic energy.

753 Expanding on the results of Ref. [12], the turbulent kinetic energy can be related to the growing mode and by
 754 extension to the mixing level γ , just as the concentration flux was in Sec. III C 1. This operation leads to two main
 755 outcomes. First, it allows to examine the energy budget and the dependency of its constitutive terms on γ . Several
 756 particular values of γ can thus be identified. Second, it allows to express the velocity of the flame center as a function
 757 of the turbulent velocity : a turbulent flame speed model can thus be formulated.

758

1. Kinetic energy, potential energy and dissipation

759 From Eq. (1b), we derive the following evolution equation for the kinetic energy $\bar{k} = \frac{1}{2} \overline{u_i u_i}$:

$$\partial_t \bar{k} + \partial_3 \left(\frac{1}{2} \overline{u_3 u_i u_i} + \overline{u_3 p} - \nu \partial_3 \bar{k} \right) = 2A_t g \overline{u_3 \bar{c}} - \bar{\varepsilon} \quad , \quad (\text{B1})$$

760 with $\bar{\varepsilon} = \overline{\nu \partial_j u_i \partial_j u_i}$ the dissipation rate of the kinetic energy. Integrating this equation over x_3 , the flux term vanishes
 761 and we are left with the following global energy budget :

$$E_K + D_K = E_P \quad , \quad (\text{B2})$$

762 where E_K is the total kinetic energy, E_P is the potential energy released into the flow and D_K is the energy dissipated
 763 into heat. These energies are hereafter defined per unit volume of the mixing zone :

$$E_K(t) = \frac{1}{H(t)} \int \bar{k}(t, x_3) dx_3 \quad , \quad D_K(t) = \frac{1}{H(t)} \int_0^t \int \bar{\varepsilon}(t', x_3) dx_3 dt'$$

$$\text{and} \quad E_P(t) = \frac{2A_t g}{H(t)} \int_0^t \int \overline{u_3 \bar{c}}(t', x_3) dx_3 dt' \quad , \quad (\text{B3})$$

764 where we recall that $H = L/\mathcal{G} > L$ measures the full extent of the turbulent mixing zone, which is larger than the
 765 front of size L where the mean concentration varies rapidly. The value of E_P can be deduced from the previous results
 766 by substituting $\overline{u_3 \bar{c}}$ with its assumed expression $F_0(L)\bar{c}(1 - \bar{c})$. In the self-similar regime, we find that:

$$E_P = (2A_t g t)^2 \times \frac{1}{24} \frac{(d_{cc} \mathcal{G}(\gamma))^2}{1 + d_{cc} \mathcal{G}(\gamma)} \quad . \quad (\text{B4})$$

767 As for the kinetic energy E_K , it can be expressed by exploiting further the assumption already introduced in Sec.
 768 III C and according to which the unstable eigenmode of the Rayleigh–Taylor instability is much larger than the other
 769 ones. As shown in [12], this assumption allows to relate not only α but also the kinetic energy to the mixing level.
 770 Extending the results of [12] to the reactive context of this study, we find that, in the self-similar regime, E_K is equal
 771 to:

$$E_K = (2A_t g t)^2 \times \frac{1}{12 d_{jj}} \frac{(d_{cc} \mathcal{G}(\gamma))^3}{(1 + d_{cc} \mathcal{G}(\gamma))^2} \quad , \quad (\text{B5})$$

772 where $d_{jj} \in [0, 1]$ is a parameter measuring the anisotropy of the turbulent structures, just as d_{cc} does. As for the
773 total dissipation D_K , its expression can be deduced from the energy budget (B2):

$$D_K = (2A_t g t)^2 \times \frac{1}{24} \frac{(d_{cc} \mathcal{G}(\gamma))^2}{1 + d_{cc} \mathcal{G}(\gamma)} \left(1 - \frac{2}{d_{jj}} \frac{d_{cc} \mathcal{G}(\gamma)}{1 + d_{cc} \mathcal{G}(\gamma)} \right) \quad . \quad (\text{B6})$$

774

2. Maximum dissipation, equipartition of energy and realisability interval

775 By linking α and β to γ , Eqs. (49)-(50) and (52)-(54) show that the knowledge of only one of these three parameters
776 is sufficient to define the asymptotic self-similar state of a reactive Rayleigh–Taylor flow. Still, they do not provide
777 any information on the value of this independent parameter. To this end, a study of the large scales of reactive
778 Rayleigh–Taylor turbulence, similar to the one performed in [17], would most probably be required. A particular
779 value of γ was nonetheless identified in the previous analysis: $\gamma_{\max} \approx 6$ is the value of γ for which β reaches its
780 maximum. This value is of course not constraining. However, it still offers a point of reference with which one may
781 assess simulation results. In this regard, the energy budget (B2) allows to identify additional particular values of γ
782 and to further map out the otherwise indiscriminate interval of γ which extends from 0 to ∞ .

783 Both E_P and E_K are decreasing functions of γ : for higher levels of mixing, less potential energy can be released
784 into the flow and less kinetic energy can be generated. As for the dissipation D_K , it is not necessarily monotonous.
785 Whenever $d_{jj} < 2 - \frac{4}{2+3d_{cc}+d_{cc}^2}$, a mild condition that is always satisfied when $d_{cc} > \sqrt{17}/2 - 3/2 \approx 0.56$, D_K reaches
786 a maximum for $\gamma = \gamma_D$ with:

$$\gamma_D = \mathcal{G}^{-1} \left(\frac{1}{2d_{cc}} \left(\sqrt{1 + \frac{16}{2 - d_{jj}}} - 3 \right) \right) \quad . \quad (\text{B7})$$

787 For the values of d_{cc} and d_{jj} observed in the simulations detailed in Sec. IV, i.e. $d_{cc} \approx d_{jj} \approx 0.55$, this maximum is
788 located at $\gamma_D = 9.4$.

789 Another point of interest corresponds to the value of γ where as much potential energy is converted into kinetic
790 energy as it is dissipated into heat. This point is reached for $E_K/E_P = 1/2$, it is to say for:

$$\gamma_{\text{equi}} = \mathcal{G}^{-1} \left(\frac{1}{d_{cc}} \frac{d_{jj}}{4 - d_{jj}} \right) \quad . \quad (\text{B8})$$

791 For $d_{cc} \approx d_{jj} \approx 0.55$, this yields $\gamma_{\text{equi}} \approx 16$. Below this value, the transfer of potential energy to E_K is predominant
792 while above it, it is the transfer to heat that is larger.

793 Let us stress that the system we are considering is not at equilibrium and that there is no reason why it should
794 settle to a maximum dissipative state. There is no reason either why an equipartition of energy transfer should exist.
795 Nonetheless, it is still interesting to point out the existence of these two particular states. Their associated γ values,
796 γ_D and γ_{equi} , can indeed serve as references for analysing simulations. In this regard, it is worth mentioning that,
797 in the non-reactive case, the total dissipation as a function of Θ_∞ reaches a maximum for $\Theta_\infty \approx 0.7$ and that the
798 equality between E_K and D_K is reached for $\Theta_\infty = 0.8$ (see Ref. [12]). In most simulations, the observed self-similar
799 value of Θ is found to lie in between those two values. Given the proximity between the reactive and non-reactive
800 cases which we have identified so far, one may wonder whether this observation also holds in the reactive case, i.e.
801 whether the asymptotic value of γ lies in between γ_D and γ_{equi} . The DNS and LES performed in Sec. IV suggest
802 that this is indeed the case : in Fig. 13, γ appear to converge to a value close to 12.

803

804 A last point we would like to mention is that not all values of γ are allowed. Indeed, the kinetic energy E_K cannot
805 exceed the potential energy E_P released into the flow. Or equivalently, the dissipation D_K must always be positive.
806 This condition may be verified for all γ provided $d_{cc} < d_{jj}/(2 - d_{jj}) < d_{jj}$. However, the expressions of d_{cc} and d_{jj}
807 obtained in [12] (Eq. (9) in this reference) suggest that we should rather have $d_{jj} \leq d_{cc}$. In that case, a constraint
808 applies on the value of γ . The latter must verify:

$$\gamma > \gamma_{\text{lim}} \quad \text{with} \quad \gamma_{\text{lim}} = \mathcal{G}^{-1} \left(\frac{d_{jj}}{d_{cc}} \frac{1}{2 - d_{jj}} \right) \quad . \quad (\text{B9})$$

809 For $d_{cc} \approx d_{jj} \approx 0.55$, we find that $\gamma_{\text{lim}} = 3.8$. Below this value, no asymptotic state based on the assumptions
810 developed in this work is possible.

3. Dynamical estimate of kinetic energy, potential energy and dissipation

The results presented so far in this appendix apply at very large times when the mixing rate Θ is asymptotically small. At intermediate times, when Θ is small but not negligible, a prediction of the kinetic energy, of the potential energy and of the dissipation rate can also be established by considering the dynamical estimates α_L , γ_L and by assuming the predominance of the Rayleigh–Taylor unstable eigenmode, as discussed in Sec. III C. In addition to this central assumption, the anisotropy constants d_{cc} and d_{jj} and the dynamic estimate γ_L are also assumed to reach a constant value at large times. Using the definition $\alpha_L = (\dot{L})^2 / (8A_t g L)$ along with Eqs. (36), (45), (50) and the relation that links the turbulent kinetic energy and concentration variance exposed in [12], one arrives at:

$$E_K = \frac{1}{48d_{jj}d_{cc}\mathcal{G}(\gamma_L)} \frac{\dot{L}^2}{1 - \Theta} \quad , \quad (\text{B10})$$

$$E_P = \frac{1 + (1 - \Theta)d_{cc}\mathcal{G}(\gamma_L)}{96d_{cc}^2\mathcal{G}(\gamma_L)^2} \frac{\dot{L}^2}{(1 - \Theta)^2} \quad . \quad (\text{B11})$$

As for the dissipation, it is deduced from Eqs. (B10) and (B11) thanks to the global energy budget (Eq. (B2)):

$$D_K = \frac{d_{jj} + (1 - \Theta)d_{cc}\mathcal{G}(\gamma_L)(d_{jj} - 2)}{96d_{jj}d_{cc}^2\mathcal{G}(\gamma_L)^2} \frac{\dot{L}^2}{(1 - \Theta)^2} \quad . \quad (\text{B12})$$

Overall Eqs. (B10), (B11) and (B12) involve Θ and γ_L , two quantities measuring the mixing level. Since our attention is focused on the dependency of E_K , E_P , D_K on γ_L , we account for the persistent influence of Θ by introducing the following dimensionless version of E_K , E_P and D_K :

$$E_K^* = (1 - \Theta) \frac{E_K}{\dot{L}^2} \quad , \quad (\text{B13})$$

$$E_P^* = (1 - \Theta)^2 \frac{E_P}{\dot{L}^2} \quad , \quad (\text{B14})$$

$$D_K^* = (1 - \Theta)^2 \frac{D_K}{\dot{L}^2} \quad . \quad (\text{B15})$$

Note that there remains an influence of Θ through higher order terms in E_P^* , D_K^* . Even so, the main advantage of introducing E_K^* , E_P^* , D_K^* is that to the main order, they are given by

$$E_K^* = \frac{1}{48d_{jj}d_{cc}\mathcal{G}(\gamma_L)} \quad , \quad (\text{B16})$$

$$E_P^* \approx \frac{1 + d_{cc}\mathcal{G}(\gamma_L)}{96d_{cc}^2\mathcal{G}(\gamma_L)^2} \quad , \quad (\text{B17})$$

$$D_K^* \approx \frac{d_{jj} + d_{cc}\mathcal{G}(\gamma_L)(d_{jj} - 2)}{96d_{jj}d_{cc}^2\mathcal{G}(\gamma_L)^2} \quad . \quad (\text{B18})$$

As can be seen, the prediction of E_K^* , E_P^* , D_K^* only involves γ_L . This makes it easier to check the consistency of Eqs. (B10), Eqs. (B11), Eqs. (B12) with simulations. Figure 14 illustrates the evolution of E_K^* , E_P^* and D_K^* with γ_L during the "self-similar" interval of time mentioned in Sec. IV D 2. The black curves in Figs. 14(a), 14(b) and 14(c) correspond respectively to the theoretical predictions Eqs. (B16), (B17) and (B18). The curves are drawn for $d_{cc} = 0.55$ and $d_{jj} = 0.52$, which are the values found in simulations. Figure 14 shows that, for LES, the trajectories followed by the simulation points are aligned with the theoretical curves. Note also that the simulation points end up concentrating in a small area centered on the values:

$$E_K^* \approx 0.2 \quad , \quad E_P^* \approx 0.3 \quad , \quad D_K^* \approx 0.1 \quad . \quad (\text{B19})$$

with $\gamma_L \approx 12$ as previously noted. Concerning the DNS, the agreement between simulation points and predictions can also be observed for the potential energy and total dissipation. Final values are roughly the same. However, a discrepancy between the evolution of kinetic energy and prediction can be noted for the case D3 and D4. A statistical effect might be at the origin of this discrepancy, but further investigation would be required to confirm this possible explanation. Note that, unlike the case D3 and D4, the case D2, shows a good agreement between the value of E_K^* computed by Eqs. (B13) and its prediction Eqs. (B16). Overall, a reasonable agreement is observed between Eqs. (B16), (B17) and (B18) and the kinetic energy, potential energy and total dissipation observed in simulations.

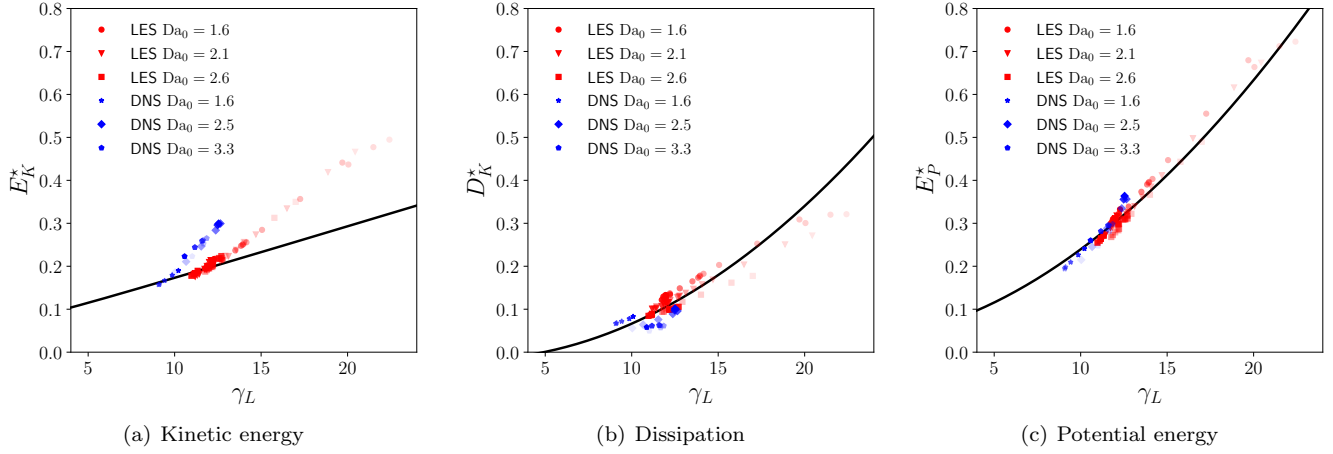


FIG. 14. Variations of E_K^* , D_K^* , E_P^* , respectively defined by Eqs. (B13), (B15) and (B14), as a function of γ_L . Comparison between simulation results (colored points) and the theoretical predictions (B16), (B18) and (B17) with $d_{cc} = 0.55$ and $d_{jj} = 0.52$ (black lines). The simulation points are plotted at different times such that $0.3 < H/L_{\text{dom}} < 0.75$ for DNS and $0.2 < H/L_{\text{dom}} < 0.75$ for LES. The timeline of the simulation is indicated by the opacity of the symbols: the more opaque, the further in time.

840

4. Flame speed

841 The flame speed associated with the displacement of the mixing zone center is defined by:

$$s_c = \dot{X}_c \quad . \quad (\text{B20})$$

842 A turbulent velocity representative of the maximum value of the kinetic energy profile is:

$$v' = \sqrt{\langle \bar{k} \rangle} = \sqrt{\frac{H}{L} E_K} \quad . \quad (\text{B21})$$

843 Using Eqs. (5), (52) and (B5), we then deduce that, at asymptotic times when Θ can be neglected, we have:

$$s_c = C_f v' \quad \text{with} \quad C_f = \sqrt{\frac{d_{jj} d_{cc}}{3} \gamma \mathcal{G}(\gamma)} \quad . \quad (\text{B22})$$

844 Thus, the burning velocity s_c scales linearly with the turbulent velocity v' in the self-similar regime. This is consistent
845 with Damköhler's theory [40].

846 As can be seen, in Fig. 15, the prefactor C_f of this proportionality law increases with γ . Note also that the prefactor
847 C_f is bounded by:

$$C_f < \sqrt{12 d_{jj} d_{cc}} \quad . \quad (\text{B23})$$

848 With $d_{cc} \approx d_{jj} \approx 0.55$, this corresponds to a maximum value of approximately 2.

850 At intermediate times, when Θ is not yet negligible, Eq. (B22) still holds but C_f is modified. The dominant mode
851 assumption (Eq. (40)) along with Eqs. (13)-(50) lead to:

$$C_f(t) = \sqrt{\frac{(1-\Theta) d_{jj} d_{cc}}{3} \gamma_L \mathcal{G}(\gamma_L)} \quad . \quad (\text{B24})$$

852 The dependency of this expression on Θ can be set apart by introducing a reduced version of the turbulent flame
853 speed:

$$s_c^* = \frac{s_c}{\sqrt{1-\Theta}} \quad . \quad (\text{B25})$$

854 This reduced flame speed s_c^* is predicted to be proportional to v' , with a constant C_f^* that depends on γ_L but not
855 on Θ :

$$s_c^* = C_f^* v' \quad \text{with} \quad C_f^* = \sqrt{\frac{d_{jj} d_{cc}}{3} \gamma_L \mathcal{G}(\gamma_L)} \quad . \quad (\text{B26})$$

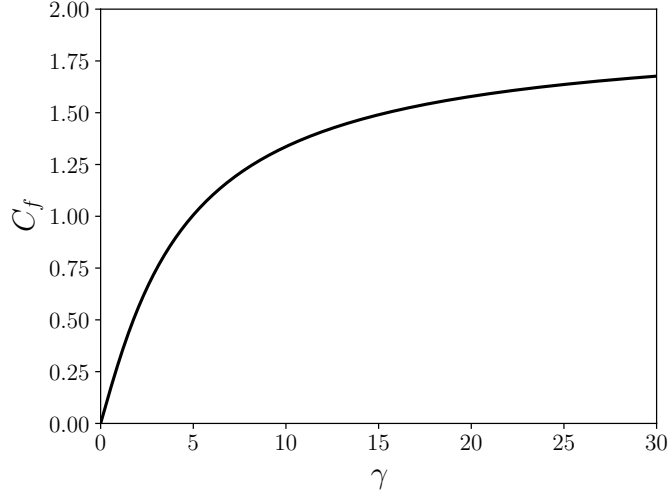


FIG. 15. Evolution of C_f with γ for $d_{cc} = 0.55$ and $d_{jj} = 0.52$.

856 Figure 16 shows the evolution of C_f^* extracted from simulations using Eq. (B25) with respect to γ_L computed with
 857 Eq. (6). The black curve corresponds to the prediction Eq. (B26). The latter is plotted for $d_{cc} = 0.55$ and $d_{jj} = 0.52$.
 858 The comparison between simulations and prediction is done for DNS, D2, D3, D4 and LES L2,L3, L4. As can be
 859 seen, the simulation points of D2, L2,L3, L4 all tends to the black curve. On the contrary, there remains a small
 860 deviation for simulation D3 and D4. This deviation is less than 15% of the value that would be obtained with Eq.
 861 (B26). To explain this deviation, there might be a statistical effect at play which is already manifest for the kinetic
 862 energy (see B 3). Even so, figure 16 seems to indicate that the result of Eq. (B26) agrees well with simulations. An
 863 another important remark that can be made is that the simulation points accumulate on a small region where the
 864 prefactor C_f^* takes the value

$$C_f^* = 1.35 \quad . \quad (B27)$$

865

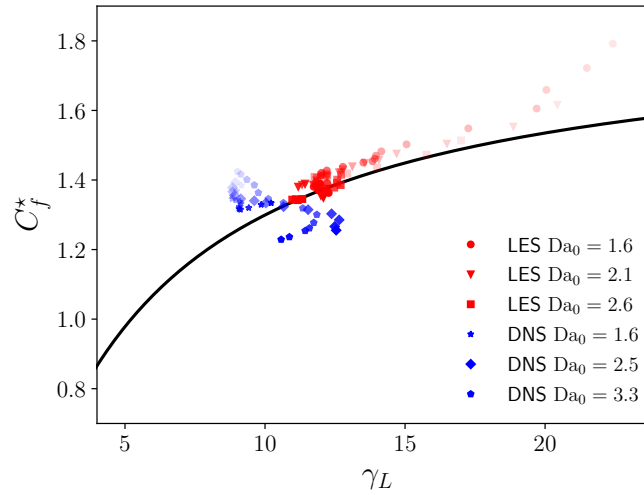


FIG. 16. Variations of $C_f^* = s_c^*/v'$, defined by Eq. (B25), as a function of γ_L . Comparison between simulation results (colored points) and the theoretical prediction (B26) with $d_{cc} = 0.55$ and $d_{jj} = 0.52$ (black lines). The simulation points are plotted at different times such that $0.3 < H/L_{\text{dom}} < 0.75$ for DNS and $0.2 < H/L_{\text{dom}} < 0.75$ for LES. The timeline of the simulation is indicated by the opacity of the symbols: the more opaque, the further in time.

866

867

868 To conclude the discussion on this topic, we would like to point out that the turbulent flame speed model determined
 869 for the self-similar regime Eq. (B22) can be recast in the form :

$$s_c = \frac{d_{cc}\gamma\mathcal{G}(\gamma)}{6\sqrt{1+d_{cc}\mathcal{G}(\gamma)}}\sqrt{2A_tgL} \approx \sqrt{0.138 \cdot 2A_tgL} \quad , \quad (\text{B28})$$

870 where the last approximation is obtained by replacing γ and d_{cc} with their asymptotic values observed in simulations.
 871 This alternative formulation of Eq. (B22) is almost similar to the one proposed in Refs. [27, 32]. However, it should
 872 be noted that, in these references, the size L_{dom} of the domain is used instead of the size L of the mixing zone. This
 873 is possible because the configuration studied in these references is confined, as opposed to the one studied here.

874

Appendix C: Source term modification

875 In this appendix, we assume that the $c(1-c)$ dependency of the F-KPP reactive source term is replaced by a
 876 general function $R(c)$ verifying:

$$\text{for } c \in]0, 1[\quad , \quad R(c) > 0 \quad \text{and} \quad R(0) = R(1) = 0 \quad . \quad (\text{C1})$$

877 In system (1), the evolution (1a) of the concentration field would then be replaced by:

$$\partial_t c + u_k \partial_k c = \nu_c \partial_{kk}^2 c + \frac{1}{\tau} R(c) \quad . \quad (\text{C2})$$

878 The core assumption of this appendix is that this substitution does not modify the main characteristics of the flow
 879 in the self-similar regime. In particular, we assume that L and X_c still grow as the square of time and that a
 880 thickened-wrinkled flame regime is reached, such that the flow becomes more and more segregated.

881 To extend the results of this work to this situation, the idea is to introduce another measure of the mixing level.
 882 Instead of Θ , we define:

$$\Theta^\diamond(t) = \frac{\int \bar{R}(x_3, t) dx_3}{\int \bar{c}(1-\bar{c})(x_3, t) dx_3} > 0 \quad . \quad (\text{C3})$$

883 This quantity is positive but has an upper bound which is not necessarily equal to 1, as opposed to Θ . Nonetheless,
 884 like Θ , Θ^\diamond tends to 0 when the mixture tends to a fully segregated state. In particular, it should verify the same
 885 self-similar asymptotic scaling as Θ , but with a different constant:

$$\text{self-similar regime : } \Theta^\diamond(t) = \gamma^\diamond \frac{\tau}{t} \quad . \quad (\text{C4})$$

886 The interest of introducing Θ^\diamond is that all the steps of the derivation detailed in the main text can be repeated by
 887 simply replacing Θ with Θ^\diamond and γ with γ^\diamond . Thus, the main predictions of this work, Eqs. (49) and (52), would
 888 become:

$$\alpha = \frac{(d_{cc}\mathcal{G}(\gamma^\diamond))^2}{1+d_{cc}\mathcal{G}(\gamma^\diamond)} \quad \text{and} \quad \beta = \frac{\gamma^\diamond (d_{cc}\mathcal{G}(\gamma^\diamond))^2}{12(1+d_{cc}\mathcal{G}(\gamma^\diamond))} \quad . \quad (\text{C5})$$

889 Their dynamic versions, Eqs.(50) and (54), would be transformed alike:

$$\alpha_L = \frac{(d_{cc}(1-\Theta^\diamond)\mathcal{G}(\gamma_L^\diamond))^2}{1+d_{cc}(1-\Theta^\diamond)\mathcal{G}(\gamma_L^\diamond)} \quad \text{and} \quad \beta_L = \frac{\gamma_L^\diamond (d_{cc}(1-\Theta^\diamond)\mathcal{G}(\gamma_L^\diamond))^2}{12(1+d_{cc}(1-\Theta^\diamond)\mathcal{G}(\gamma_L^\diamond))} \quad , \quad (\text{C6})$$

890 with $\gamma_L^\diamond(t) = 2\Theta^\diamond(t)\frac{\tau_L(t)}{\tau}$.

891 The comparison with the main text results can be pushed further by introducing an additional hypothesis. The
 892 probability density function (PDF) of a scalar bounded between 0 and 1 is usually well described by a β -PDF. We
 893 assume that this is the case for reactive Rayleigh–Taylor turbulence, that is to say, we assume that the PDF of c is:

$$f_\beta(c) = \frac{c^{a-1}(1-c)^{b-1}}{B(a,b)} \quad \text{with} \quad a = \bar{c}\frac{\overline{c(1-c)}}{c^2} \quad , \quad b = (1-\bar{c})\frac{\overline{c(1-c)}}{c^2} \quad , \quad B(a,b) = \int_0^1 c^{a-1}(1-c)^{b-1} dc \quad . \quad (\text{C7})$$

894 The function $B(a,b)$ is the β -function and is equal to $\Gamma(a)\Gamma(b)/\Gamma(a+b)$, with Γ the extension of the factorial to
 895 positive reals. In the limit $\Theta \ll 1$ and with the assumption that $\overline{c(1-c)}$ varies like $\bar{c}(1-\bar{c})$, the two parameters a
 896 and b tend to:

$$\text{for } \Theta \ll 1 \quad , \quad a \approx \bar{c}\Theta \quad \text{and} \quad b \approx (1-\bar{c})\Theta \quad . \quad (\text{C8})$$

897 As a result, the average of R can be expressed as:

$$\text{for } \Theta \ll 1 \quad , \quad \bar{R} = \int_0^1 R(c) f_\beta(c) dc \approx \frac{\mathcal{R}(\bar{c}, \Theta)}{B(\bar{c}\Theta, (1-\bar{c})\Theta)} \quad \text{with} \quad \mathcal{R}(\bar{c}, \Theta) = \int_0^1 R(c) c^{a-1} (1-c)^{b-1} dc \quad . \quad (\text{C9})$$

898 For small values of Θ , the β -function $B(a, b)$ diverges as:

$$\text{for } \Theta \ll 1 \quad , \quad B(a, b) \approx [\bar{c}(1-\bar{c})\Theta]^{-1} \quad . \quad (\text{C10})$$

899 By contrast, with $R(0) = R(1) = 0$, the integral $\mathcal{R}(\bar{c}, \Theta)$ tends to a finite value:

$$\text{for } \Theta \ll 1 \quad , \quad \mathcal{R}(\bar{c}, \Theta) \approx \mathcal{R}(\bar{c}, 0) \quad . \quad (\text{C11})$$

900 Therefore, injecting the above expression into the definition of Θ^\diamond , one deduces that

$$\text{for } \Theta \ll 1 \quad , \quad \bar{R} \approx \Theta \bar{c}(1-\bar{c}) \mathcal{R}(\bar{c}, 0) \quad , \quad (\text{C12})$$

901 and that

$$\text{for } \Theta \ll 1 \quad , \quad \Theta^\diamond \approx \eta^\diamond \Theta \quad \text{with} \quad \eta^\diamond = \frac{\int \bar{c}(1-\bar{c}) \mathcal{R}(\bar{c}, 0) dx_3}{\int \bar{c}(1-\bar{c}) dx_3} \quad . \quad (\text{C13})$$

902 Thus, Θ and Θ^\diamond are proportional to one another, with a prefactor that depends on the shape $R(c)$ of the source term
903 and that can be determined analytically or numerically depending on the complexity of $R(c)$. This proportionality
904 relationship can be used to replace Θ^\diamond and γ^\diamond in Eqs. (C5) and (C6). One finds that:

$$\alpha = \frac{(d_{cc} \mathcal{G}(\eta^\diamond \gamma))^2}{1 + d_{cc} \mathcal{G}(\eta^\diamond \gamma)} \quad \text{and} \quad \beta = \frac{\eta^\diamond \gamma (d_{cc} \mathcal{G}(\eta^\diamond \gamma))^2}{12 (1 + d_{cc} \mathcal{G}(\eta^\diamond \gamma))} \quad , \quad (\text{C14a})$$

$$\alpha_L = \frac{(d_{cc}(1-\eta^\diamond \Theta) \mathcal{G}(\eta^\diamond \gamma_L))^2}{1 + d_{cc}(1-\eta^\diamond \Theta) \mathcal{G}(\eta^\diamond \gamma_L)} \quad \text{and} \quad \beta_L = \frac{\eta^\diamond \gamma_L (d_{cc}(1-\eta^\diamond \Theta) \mathcal{G}(\eta^\diamond \gamma_L))^2}{12 (1 + d_{cc}(1-\eta^\diamond \Theta) \mathcal{G}(\eta^\diamond \gamma_L))} \quad . \quad (\text{C14b})$$

905 To illustrate how η^\diamond depends on the shape of R , we may look at the particular case where R varies like:

$$R(c) = c^m (1-c)^n \quad . \quad (\text{C15})$$

906 Then, in the limit $\Theta \ll 1$, we have $\bar{R} = \bar{c}(1-\bar{c})\Theta B(m, n)$ so that η^\diamond is equal to:

$$\eta^\diamond = B(m, n) \quad . \quad (\text{C16})$$

907 With m and n decreasing below 1, the profile of $R(c)$ becomes flatter than in the F-KPP case ($m = n = 1$) (ultimately,
908 it tends to a step-like profile when m and n tend to 0). In that case, Eq. (C16) shows that η^\diamond becomes larger than 1
909 and increases as m and n decrease. For a given level of mixing measured by γ , α is then smaller than in the F-KPP
910 case. By contrast, with m and n increasing above 1, the profile of $R(c)$ becomes more peaked and η^\diamond decreases. For
911 a given level of mixing measured by γ , α is then higher than in the F-KPP case.